Research Square

Preprints are preliminary reports that have not undergone peer review.
They should not be considered conclusive, used to inform clinical practice,
or referenced by the media as validated information.

Direct observations reveal cloud amplification of Arctic surface longwave warming

Benjamin Riot-Bretêcher

benjamin.riotbretecher@mail.mcgill.ca

McGill University https://orcid.org/0009-0009-6531-7555

Yi Huang

McGill University https://orcid.org/0000-0002-5065-4198

Physical Sciences - Article

Keywords:

Posted Date: August 5th, 2026

DOI: https://doi.org/10.21203/rs.3.rs-10397517/v1

License: This work is licensed under a Creative Commons Attribution 4.0 International License.
Read Full License

Additional Declarations: There is **NO** Competing Interest.

Direct observations reveal cloud amplification of Arctic surface longwave warming

Author Information

Affiliations

Department of Atmospheric and Oceanic Sciences, McGill University, Montreal, Québec, Canada[1]

Benjamin Riot-Bretêcher[1], Yi Huang[1]

Contributions

Y.H. conceived the study and acquired the funding. B.R.B. developed the numerical workflow, performed the multivariate spectral analysis, and derived the surface radiative fluxes. B.R.B. performed the analysis of the results. B.R.B. wrote the first draft of the manuscript, and Y.H. contributed to the revision and final editing.

Corresponding author

Correspondence to: Benjamin Riot-Bretêcher[1] (benjamin.riotbretecher@mail.mcgill.ca)

Abstract

The Arctic has warmed considerably faster than the global average, with consequences for sea ice, permafrost and mid-latitude weather[1], yet the radiative feedback mechanisms behind the warming amplification remain poorly constrained by observations[2]. Determining feedback magnitudes from radiation flux measurements is difficult because they blend the effects of many factors including atmospheric temperature, moisture, clouds and greenhouse gases[3,4]. Here we apply a spectral fingerprinting method[3,5–8] to long-term measurements of spectrally resolved downwelling longwave radiance at the North Slope of Alaska, isolating individual longwave forcings and feedbacks using their distinct spectral signatures. We find a positive surface longwave cloud feedback of 1.10 ± 0.93 W m^{-2} per decade, which strongly amplifies surface warming at this Arctic site and contrasts starkly with the

negative feedback documented at mid-latitudes[8]. These findings identify cloud feedback as an important amplifier of Arctic surface warming, suggesting a fundamental asymmetry in cloud feedbacks between high and mid latitudes that many climate models fail to capture.

Introduction

The roles of different physical mechanisms driving the rapid warming of the Arctic—a phenomenon known as Arctic Amplification—remain poorly quantified[2,9]. Consequently, this region exhibits one of the largest spreads in projected warming among climate models. This divergence is largely caused by the uncertainties in cloud feedbacks[10,11]—the amplification or damping of surface warming through changes in clouds—and their impact on the energy budget. Quantifying clouds' role and especially in terms of the surface energy balance is a grand challenge, as satellite measurements in the Arctic generally struggle to resolve surface fluxes beneath clouds[12,13], an observational gap targeted by upcoming space missions[14–16].

The broadband radiation flux measurements of ground-based radiometers have indicated that the downwelling longwave radiation (DLR) at the surface is increasing[17,18]. However, such broadband fluxes face two fundamental limitations as a constraint on Arctic longwave feedbacks. First, the spectrally integrated measurements cannot separate the total change into temperature, water vapour, cloud, and greenhouse-gas components—the decomposition needed to isolate their radiative feedbacks. Second, the difficulty to assure their radiometric accuracy, exacerbated in harsh polar environments[19,20], makes it challenging to detect long-term trends. In comparison, the Atmospheric Emitted Radiance Interferometer[21,22] (AERI), a high-resolution spectrometer with radiometric accuracy traceable to SI standards, overcomes these difficulties. Its high accuracy ensures that real atmospheric radiation trends can be detected against instrumental artefacts, while its high spectral resolution resolves the distinct signatures of individual radiative drivers, allowing their radiative feedbacks to be quantified separately[4,8].

At the North Slope of Alaska (NSA) site of the Department of Energy Atmospheric Radiation Measurement (ARM) program, an Extended-range AERI (E-AERI) instrument has been recording the DLR spectrum for more than two decades[23,24]. The Arctic atmosphere presents unique conditions where

clouds exert primary control of the surface radiation budget[12,24–26]. Broadband radiation flux measurements have indicated an increase in cloud opacity[18], which makes the Arctic atmosphere less transmissive[17]. While previous works utilizing E-AERI records evidenced an increase of DLR under all-sky conditions[24] and the radiative forcing of greenhouse gases[3], a comprehensive quantification of year-round, all-sky feedback to the surface longwave budget remains lacking.

To disentangle overlapping contributions to the DLR changes, we utilized the optimal spectral fingerprinting method[3,5–8]. This technique separates the radiative impacts of individual atmospheric variables including atmospheric temperature, carbon dioxide, water vapour, ozone, methane, and clouds, by leveraging their distinct spectral signatures and quantifying their contributions to the total radiance change via a multivariate regression[3]. This method was applied to AERI measurements in the mid-latitudes, revealing a negative surface longwave cloud feedback that damps surface warming over land[8,27]. By deploying this fingerprinting framework at the NSA site, we establish an observational benchmark of cloud surface longwave feedback in the Arctic region and make a direct comparison to the lower latitudes to identify mechanisms driving Arctic Amplification.

Crucially, although this method requires cloud microphysical information to perform radiative transfer calculations, these data are only used to identify the spectral shape (fingerprint) of cloud feedback, without making *a priori* assumptions about its magnitude. The magnitudes of cloud feedback and other drivers are instead determined by directly regressing the measured spectral radiance change to the normalized fingerprints—bypassing the need for accurate, homogenized multidecadal records of cloud microphysical properties, which are currently lacking due to the inherent uncertainties of cloud retrieval algorithms and the inter-dataset discrepancies resulted[28,29]. To account for the structural uncertainties in cloud information such as vertical distribution and phase partitioning, we evaluated our framework across a comprehensive ensemble of cloud profiles and optical depth perturbation scenarios. We found the cloud spectral fingerprint to be robust, with its spectral shape remaining essentially invariant to the choices of microphysical datasets and perturbation magnitudes (Extended Data Fig. 1). By applying this framework

to the long-term E-AERI record, we isolated the individual surface longwave forcing and feedback contributions, providing an observational constraint of Arctic Amplification mechanisms.

Results

Spectral Radiance Trends

The North Slope of Alaska is one of the cloudiest places on Earth, with cloud occurrence exceeding 80%[12]. This persistence heavily influences the radiance trend determination; the scarcity of clear-sky instances renders clear-sky DLR trends statistically insignificant[24]. In contrast, the observed all-sky DLR trends (Fig. 1a, black line) are prominent and exhibit a distinct spectral structure: strong positive radiance changes are observed in the water vapour rotation band (below 600 cm^{-1}), the carbon dioxide vibration-rotation band (centred at 667 cm^{-1}), the atmospheric window (800–1200 cm^{-1}) and the water vapour vibration-rotation band (centred at 1594 cm^{-1}). Prominent positive trends across the mid- and far-infrared (FIR) indicate that all radiative drivers act in concert to increase the DLR at this site[24]—a pattern that qualitatively differs from the mid-latitudes, where cloud changes induce negative trends in the atmospheric window[8,27].

After confirming that our radiative transfer simulations accurately reproduced the observed atmospheric variability (Extended Data Fig. 2), we applied the optimal fingerprinting method to explain the all-sky DLR trends. The reconstructed radiance changes agree well with observations, with residuals generally within 1 radiance unit (RMS = 0.25 RU, $R^2 = 0.93$; Fig. 1a) across the mid-infrared and slightly larger in the carbon dioxide R-branch wing (690–750 cm^{-1}) and the FIR (420–590 cm^{-1}), where the trend uncertainty is relatively larger. Note that the FIR channels with small signal-to-noise ratios are not included in the fingerprinting (see Methods; Extended Data Fig. 3d, e).

Using this framework, we attributed the all-sky DLR spectral change to these drivers: temperature, water vapour, ozone, carbon dioxide, methane, and clouds (Fig. 1b). Each driver induces a spectrally distinct DLR change. Temperature warming drives radiance increases across the whole spectrum, with the largest contributions in the water vapour and carbon dioxide absorption bands where the atmosphere is optically thick. Cloud changes produce positive spectral changes primarily in the atmospheric window—a signature of increasing cloud optical depth—and also in the FIR (dirty window). Water vapour increases contribute to spectral increases in its rotation band and relatively weakly in the atmospheric window, while carbon dioxide and methane contribute to spectral increases in their respective absorption bands (centred at 667 cm^{-1} and 1306 cm^{-1}, respectively). Ozone contributes a small negative change near 1040 cm^{-1}. These spectral attributions form the basis for the quantitative flux analysis in the following section.

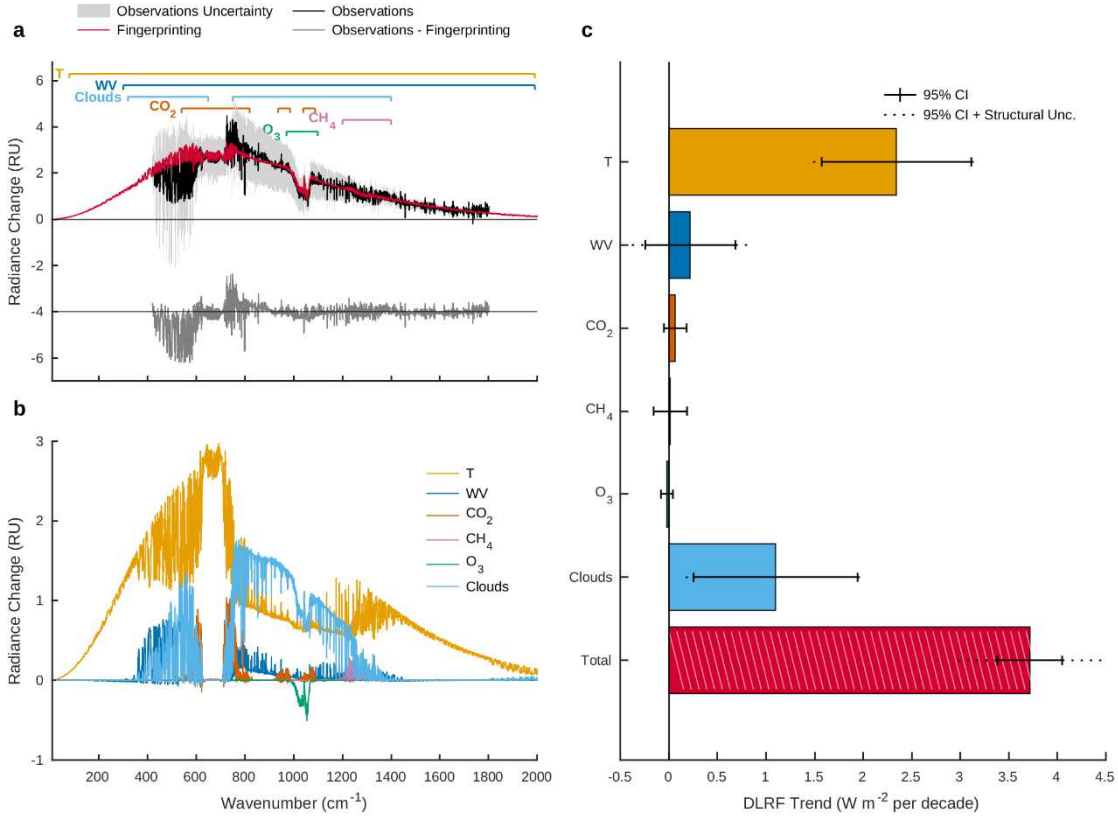


Fig. 1: Decomposition of the DLR spectral changes at the NSA site. a, Observed (black) and reconstructed (red) spectral radiance changes at the NSA site for the 26-year period (1998–2023). The grey line shows the residuals (observed minus reconstructed), offset by 4 RU for visual clarity. Grey shading indicates the 1σ observational uncertainty. Horizontal bars at the top of the panel denote the spectral ranges subject to the influence of each contributor. **b,** Spectral decomposition of the total long-

term change into individual contributions by atmospheric temperature (T), water vapour (WV), carbon dioxide (CO_2), methane (CH_4), ozone (O_3), and clouds derived via optimal fingerprinting. Radiance values are plotted in Radiance Units (RU), where 1 RU = mW / (m^2 sr cm^{-1}). **c,** The total downwelling longwave radiation flux trend ("Total") over the 26-year observational period decomposed to contributions of each component. Solid lines denote the 95% confidence intervals associated with statistical uncertainties (including optimal fingerprinting, E-AERI observations, and non-linearity, as shown in Extended Data Fig. 11). Dashed lines represent the extended uncertainty range following quadrature addition of the structural penalty from the unattributed FIR spectral residual (see Methods).

Individual Forcing and Feedback Contributions

The scaling factors determined from the spectral fingerprinting directly quantify the energetic contribution of each driver across the full longwave spectrum. Converting these spectral attributions to broadband radiative flux requires a conversion factor $\kappa(\nu)$ derived from accurate line-by-line radiative transfer computations, which accounts for the angular anisotropy between the E-AERI zenith radiance and hemispheric irradiance (see Methods and Extended Data Fig. 4). This yields component contributions to the total downwelling longwave radiation flux (DLRF) trend over the 26-year observational period (Fig. 1c; Extended Data Table 1). The total DLRF trend amounts to 3.72 ± 0.74 W m^{-2} per decade (all uncertainties represent 95% confidence intervals combining statistical uncertainty and a structural penalty from the unattributed FIR flux; see Methods), consistent in sign with broadband longwave increases recently documented at this site[17,18].

Atmospheric warming makes the largest contribution to the DLRF trend: 2.35 ± 0.86 W m^{-2} per decade. This temperature contribution shows a spectral pattern (Fig. 1b) that reflects strong Arctic warming largely confined to the surface and the lower troposphere. This contribution encompasses the effects of the Planck and lapse rate feedbacks in the conventional climate feedback decomposition framework[9,30]. It is worth noting that although this contribution is of the largest magnitude at the NSA site, it does not qualitatively differ from that at the mid-latitudes[8]. Hence, the temperature-driven DLRF change represents Arctic Amplification itself rather than revealing the cause of it.

Cloud feedback emerges as the second largest contributor, yielding a positive DLRF trend of 1.10 ± 0.93 W m^{-2} per decade, driven by increasing cloud opacity at NSA. This stands in stark contrast to the mid-latitudes, where the same fingerprinting framework[8] reveals a negative surface longwave cloud feedback of -1.77 ± 2.31 W m^{-2} per decade, driven by decreasing low cloud cover there. Normalizing by the local surface warming rate of 0.78 K per decade[24], this yields a longwave cloud feedback parameter of 1.41 ± 1.19 W m^{-2} K^{-1} in the Arctic, in contrast to a -3.93 ± 5.13 W m^{-2} K^{-1} counterpart found at the mid-latitudes[8] (Fig. 2) . The reversal of sign reflects fundamentally different cloud feedbacks to surface warming: at mid-latitudes, warming leads to reduction in low cloud cover and DLR, whereas in the Arctic, increasing cloud optical depth increases DLR and amplifies the surface warming. The finding here identifies the cloud longwave feedback as a primary cause of the enhanced surface longwave warming at NSA relative to mid-latitudes (Fig. 2).

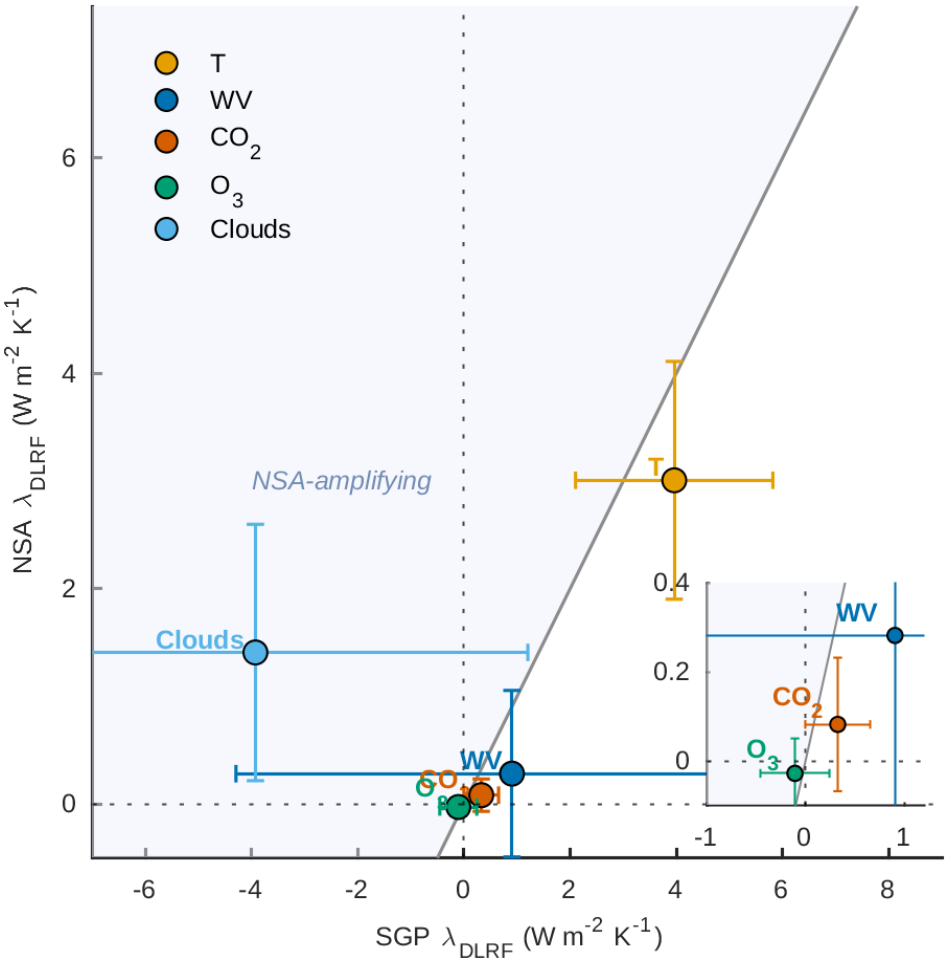


Fig. 2: Cloud longwave feedback accounts for the warming amplification in the Arctic relative to mid-latitudes. Comparison of the local downwelling longwave radiation flux feedback parameter (λ_{DLRF}) at the NSA against the Southern Great Plains (SGP) site for individual components. The feedbacks (T, WV, Clouds) parameters and normalized forcings (CO_2, O_3) are derived by dividing the component decadal DLRF trends by the local surface warming trends (dT_s = 0.78 K per decade at NSA[24]; 0.45 K per decade at SGP[8]). The solid grey line indicates the 1:1 relationship. The blue shaded region denotes the "Arctic-Amplification" regime, where the per-kelvin downwelling longwave response is stronger in the Arctic than at mid-latitudes, thus contributing to more warming in the Arctic. The bottom-right inset provides a magnified view of the trace gas and water vapour components near the origin. Error bars represent 95% confidence intervals. Note CH_4 is not shown because it was not included in ref.[8].

Water vapour contributes a positive DLRF trend of 0.22 ± 0.60 W m^{-2} per decade, consistent with the observed Arctic moistening over the study period, although the signal does not reach statistical significance at the 95% confidence level. Independent validation using ERA5 radiative kernels[31,32]

confirms a positive water vapour contribution: 0.51 ± 0.27 W m^{-2} per decade, as well as a temperature contribution: 3.77 ± 1.29 W m^{-2} per decade. Both estimates exceed the fingerprinted magnitudes (Extended Data Fig. 5), which is physically expected: the kernel method sums radiative contributions from each atmospheric layer assuming that they are independent and neglecting the masking of upper-level signals by lower-layer water vapour and clouds—an effect that is particularly pronounced at NSA given the high occurrence of low clouds there. A similar overestimation by the kernel method relative to optimal fingerprinting was documented before[8].

The methane contribution is found to be 0.01 ± 0.17 W m^{-2} per decade and the ozone contribution -0.02 ± 0.06 W m^{-2} per decade. The carbon dioxide forcing is 0.06 ± 0.12 W m^{-2} per decade.

Fingerprinting the sparse clear-sky subset[24] (conditions occurring less than 20% of the time) yielded a clear-sky DLRF trend of 2.82 ± 0.66 W m^{-2} per decade and a carbon dioxide contribution of 0.24 ± 0.33 W m^{-2} per decade (Extended Data Fig. 6c; full component breakdown in Extended Data Table 1), consistent with the surface forcing from rising carbon dioxide reported earlier for this site[4]. That the all-sky carbon dioxide forcing is smaller than the clear-sky value reflects cloud masking: prevailing optically thick clouds at NSA saturate the atmospheric emissivity, substantially attenuating the DLRF sensitivity to rising carbon dioxide concentrations.

Regional Context

Although the fingerprinting analysis is anchored to a single ground site, the finding above is representative of Arctic cloud-radiation interactions. Located at the intersection of sea ice and continental climate regimes, the NSA site samples air masses advected from a wide oceanic area due to prevailing northerly winds[33], and has been shown to sample a broad range of meteorological conditions representative of the wider Arctic[18,33]. Surface longwave CRE trends from the ERA5 reanalysis[34,35] over the Arctic (60°–90°N) for the 1998–2023 period (Fig. 3a) show generally positive trends over the Arctic Ocean, with a value of 0.49 ± 0.79 W m^{-2} per decade at NSA, consistent in sign with the CRE derived

from E-AERI observations (0.90 ± 1.03 W m^{-2} per decade; all-sky minus clear-sky). This is in sharp distinction from the negative surface longwave CRE trends documented over mid-latitude continental regions[8], confirming that the sign reversal of cloud feedbacks between the Arctic and the lower latitudes is not specific to the NSA site but reflects a fundamental asymmetry across latitudes. Splitting both domains into land and ocean sub-domains using the ERA5 land-sea mask, this sign reversal persists even when comparing ocean surfaces alone (Arctic Ocean +0.19 ± 0.26 versus 60°S–60°N ocean -0.22 ± 0.05 W m^{-2} per decade), ruling out a land-ocean contrast as the explanation. Examination of the interannual time series further shows that CRE anomalies at NSA correlate with the Arctic-mean anomalies (r = 0.50).

The spatial pattern of the CMIP6 ensemble-mean CRE trend broadly resembles that of ERA5, with both showing a coherent band of positive trends across the Arctic Ocean (Fig. 3a, b). There are also significant correlations between the NSA site and the Arctic average (60°–90°N) in both CRE and DLRF trends (r = 0.60 and 0.65, respectively, *p-value* < 0.01) in the CMIP6 models[36] (Fig. 4a, b; Extended Data Table 2). Many climate models, however, fail to capture the magnitude of the E-AERI-measured CRE trend (Fig. 4a), indicating they underestimate the positive surface longwave radiative feedback of clouds. Excluding the temperature-driven DLRF trend that is set by each model's surface warming rate (r = 0.95; Extended Data Fig. 7b), the inter-model disagreement resides largely in the non-temperature (cloud) component of the DLRF trend (r = 0.84; Extended Data Fig. 7c). The E-AERI CRE trend measures this cloud term directly, without regression against the warming rate. It therefore discriminates among models, excluding the 9 of 23 that simulate negative trends (Extended Data Table 2). This cloud term also covaries with the net surface longwave trend (Extended Data Fig. 7d), so the discrimination bears directly on the simulated surface energy budget. NSA's CRE trend itself correlates only moderately with local warming (r = 0.50; Fig. 4c), showing that models are not excluded simply because they warm more slowly. The excluded models instead appear to misrepresent Arctic cloud optical-depth microphysics, plausibly reflecting known biases in mixed-phase cloud parameterizations[25,37].

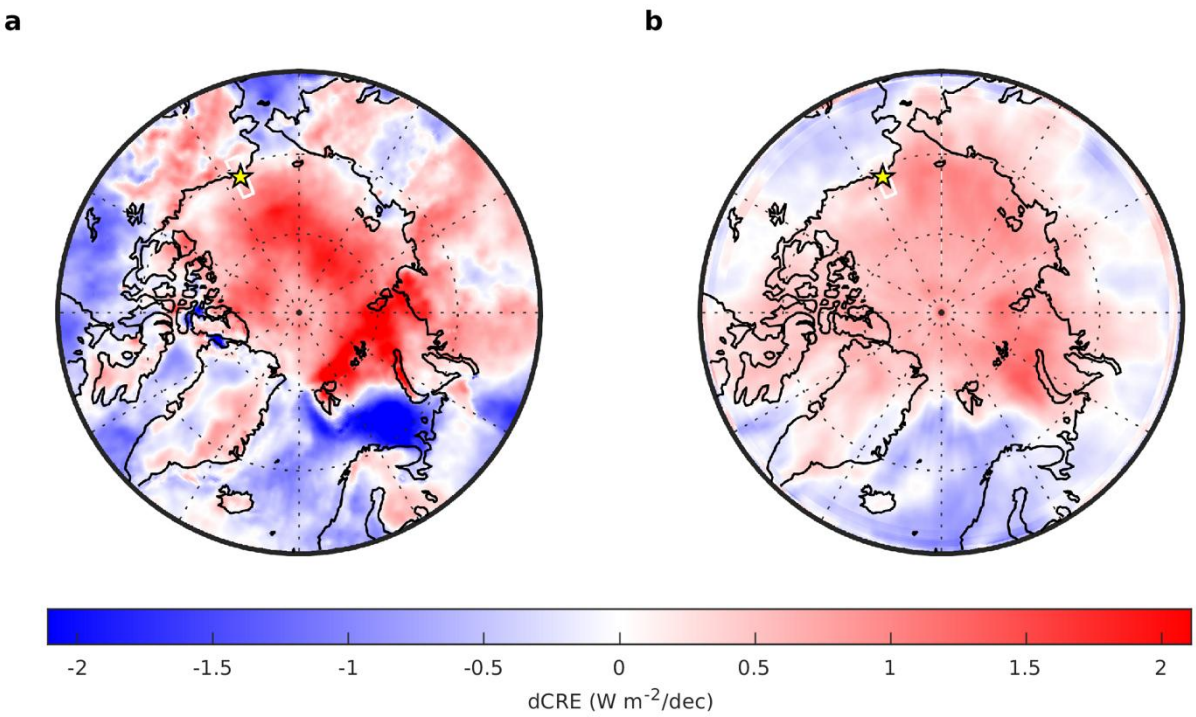


Fig. 3: Regional context of the NSA surface longwave trends. a, Trends in surface downwelling longwave cloud radiative effect (CRE, defined as all-sky minus clear-sky downwelling longwave flux) over 60°–90°N for the period 1998–2023, derived from ERA5 reanalysis[34,35]. **b,** Corresponding ensemble-mean CRE trend from the 23-model CMIP6 historical ensemble over 1998–2014 (Extended Data Table 2). In **a** and **b**, the yellow star marks the NSA site, and the white box indicates the ±2.5° latitude-longitude box used to compute the NSA average.

The "observation-constrained" global datasets also show noticeable discrepancies from the E-AERI measurements in DLRF and CRE trends. As summarized in Extended Data Fig. 7a and 8, ERA5 (0.49 ± 0.79 W m^{-2} per decade) shows a positive CRE trend, agreeing with E-AERI in sign, while CERES (-0.29 ± 0.81 W m^{-2} per decade, 2000–2023) and MERRA-2 (-1.04 ± 0.67 W m^{-2} per decade, 1998–2023) show negative trends. This underscores the substantial uncertainty of gridded datasets in the surface radiation budget, which requires more benchmark radiation measurements such as E-AERI to evaluate.

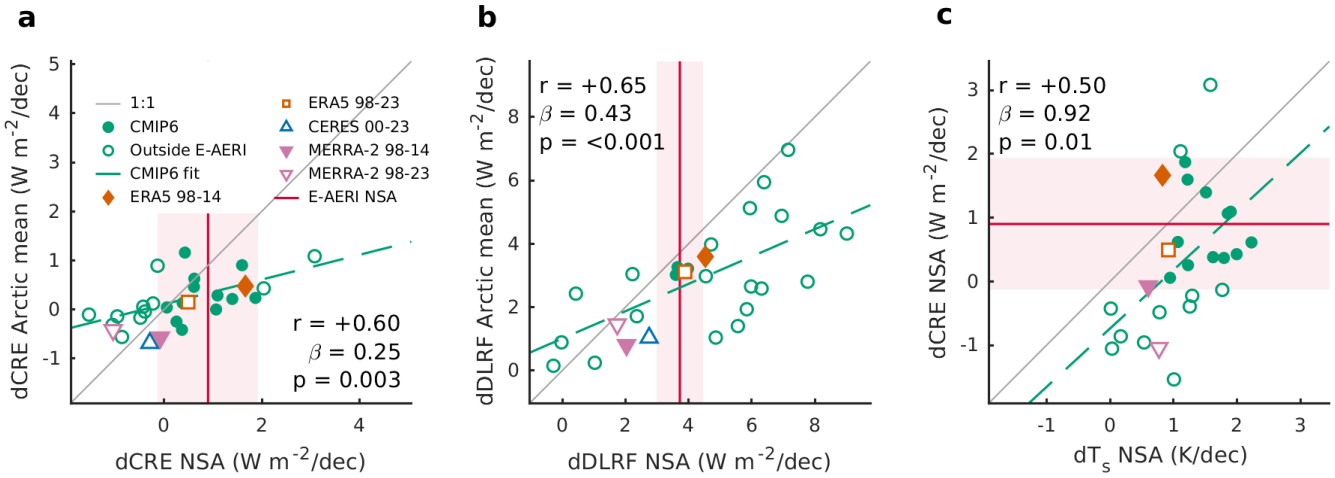


Fig. 4: Using NSA to discriminate among CMIP6 models. a, Per-model decadal trends at NSA versus the Arctic mean (60°–90°N) for CRE. **b**, Same but for all-sky DLRF. **c**, Per-model decadal CRE trend at NSA versus the corresponding near-surface warming rate (dT_s NSA). The dashed green line is the across-model linear fit and the grey line is the 1:1 relation. Filled teal circles denote CMIP6 models whose NSA trend (dCRE NSA in **a**, **c**; dDLRF NSA in **b**) falls within the E-AERI 95% confidence interval (shaded band); open teal circles denote models falling outside it. Diamonds, squares, and inverted triangles denote ERA5 and MERRA-2 trends, respectively; filled markers indicate the 1998–2014 window (matching the CMIP6 ensemble) and open markers indicate the full 1998–2023 record. Upward triangles show CERES EBAF, available only for the period 2000–2023. The correlation coefficient r, slope β, and *p-value* are included in each panel.

Discussion

The application of spectral fingerprinting to 26 years' E-AERI observations at NSA reveals that Arctic cloud changes act as an important amplifier of surface longwave warming, yielding a positive cloud feedback of 1.10 ± 0.93 W m^{-2} per decade, in stark contrast to the negative feedback found at mid-latitudes[8]. This sign reversal reflects a fundamental asymmetry in how clouds respond to warming across latitudes. At mid-latitudes, warming reduces low cloud cover, diminishing the DLR and thus partially damping the surface warming[8]. In the Arctic, a dominant cloud response is an increase in cloud optical

depth, driven partly by increasing liquid water path as temperatures rise[18], and partly by the expansion of open-ocean moisture sources associated with sea ice loss[17]. These mechanisms act to increase DLR and amplify the surface warming, explaining Arctic Amplification.

A positive surface longwave cloud feedback, which many models underestimate, has a direct consequence for climate projections: models biased toward negative or weak Arctic CRE trends will systematically underestimate Arctic Amplification, particularly in the cold season when this longwave component dominates. The E-AERI constraint offers a benchmark for diagnosing and correcting such biases, which likely originate in the representation of Arctic cloud microphysics[25,37]. Whether doing so would narrow the well-known spread in projected Arctic warming[2] is an open and important question.

We find that the co-located ARM pyrgeometer measurements[38] yield a larger broadband trend of 6.22 $\pm$ 2.60 W m^{-2} per decade over 2003–2023 (see Methods), consistent in sign but providing a weaker constraint owing to its larger absolute radiometric uncertainty. This elevated trend is difficult to reconcile with the E-AERI radiances. Independently, the water vapour trends from ARMBE[39] and ERA5[40] datasets propagated through radiative transfer, would on their own (without adding any cloud or temperature contribution) produce radiance changes far exceeding those observed by E-AERI in the FIR (Extended Data Fig. 9). In comparison, the spectrally fingerprinted feedbacks are based on the measured radiance with SI-traceable accuracy, rather than geophysical variable datasets lacking independent, SI-traceable calibration.

This study addresses the longwave surface energy budget, which dominates the Arctic surface cloud radiative effect and warms the surface in the annual mean[12]. Because shortwave is absent during the polar night, clouds induce pure longwave warming in the cold season—when Arctic Amplification is most prominent[9,41]—so the longwave cloud feedback quantified here is its most relevant component. The optical-depth increase driving this feedback also reduces atmospheric shortwave transmission, so the net cloud feedback is likely smaller than the longwave signal alone, although its magnitude has yet to be quantified by direct observation.

The feedback analysis established here represents, to the best of our knowledge, the first direct spectral quantification of a surface longwave cloud feedback in the Arctic. This provides an observational benchmark against which climate models can be evaluated to reliably project warming in this most rapidly changing region on Earth. Continuing the E-AERI record is essential to ensuring this valuable observational constraint remains available for assessing future climate models. Satellite missions employing similarly high spectral-resolution and high radiometric accuracy radiance measurements[42] may provide complementary constraints from the space perspective, which merits future investigation.

Methods

The E-AERI instrument measures the downwelling longwave radiance spectrum at high spectral resolution (comprehensive quality-control procedures are detailed in ref.[24]). To mitigate the effects caused by diminished detector responsivity at the band edges[21,22], spectral channels outside the 420–1700 cm^{-1} range are excluded from the analyses here.

Spectral fingerprint calculations

Following ref.[8], spectral fingerprints of the relevant forcing and feedback factors are characterized using the partial radiative perturbation (PRP) method[43]. We extracted these fingerprints by simulating the DLR spectrum across the mid- and far-infrared (10-2000 cm^{-1}) using the Line-by-Line Radiative Transfer Model (LBLRTM)[44] coupled with the Discrete Ordinates Radiative Transfer Program (DISORT)[45]. Forward model inputs included vertical profiles of atmospheric temperature, cloud optical depth (COD), and radiatively active gases (H_2O, CO_2, CH_4, O_3, CCl_4, CFC-11, CFC-12, CO, and N_2O).

Hourly profiles of temperature and specific humidity were obtained from the ERA5 reanalysis dataset[34,40] for the grid box encompassing the North Slope of Alaska (NSA) site in Utqiaġvik. O_3 profiles were obtained from MERRA-2 reanalysis dataset[46]. Hourly vertical profiles of CO_2 and CH_4 were derived from the CarbonTracker dataset[47], supplemented by NOAA Global Monitoring Laboratory (GML) surface observations[48,49] when profile data were temporarily unavailable. The remaining well-mixed trace gases

(CCl_4, CFC-11, CFC-12, CO, and N_2O) were prescribed as vertically uniform profiles using monthly mean surface measurements from the NOAA GML long-term observatory[50].

Accounting for the presence of thin ice and mixed-phase clouds, COD was computed at a high spectral resolution of 1 cm^{-1} using an open-source optics parameterization for clouds and precipitation[51], built on the ice-particle single-scattering database of ref.[52]. Cloud microphysical properties used in the optical depth calculation were obtained from the Department of Energy Atmospheric Radiation Measurement (ARM) MICROBASE retrieval products[53] for the NSA site. Time slices lacking valid cloud retrievals (17.4%) were removed from the analysis.

To establish a representative base climate state, we constructed atmospheric profiles from a neutral reference year (2003) with respect to long-term average. We performed sensitivity tests using an alternative neutral year (2013) to ensure results were not biased by the choice of reference state (Extended Data Fig. 10). The derived spectral fingerprints from the two baseline years exhibit exceptionally high cross-correlation ($r > 0.99$), confirming that these spectral fingerprints are independent of baseline year choice.

Following ref.[8], the spectral fingerprint $\mathbf{S}_{x,t}$ of a variable x is defined as its radiance response normalized by the spectrally integrated radiant energy change:

$$\mathbf{S}_{x,t} = \frac{\mathbf{R}(x+\Delta x) - \mathbf{R}(x)}{\int_{\nu_1}^{\nu_2} [\mathbf{R}(x+\Delta x) - \mathbf{R}(x)] d\nu} \quad (1)$$

where $\mathbf{R}$ is the DLR from the forward model and Δx is the vertically resolved 26-year change, integrated over 10–2000 cm^{-1}. The multidecadal changes (Δx) for each climate driver were determined using linear trends of their respective monthly-mean anomalies over the 1998–2023 period. The ARM Best Estimate (ARMBE) dataset[39] was used to derive the temperature and water vapour changes. Temperature trends were computed using annual mean anomalies, whereas specific humidity trends were computed for every season to account for strong intra-annual variability. Sensitivity tests using seasonal and monthly rather than annual-mean temperature trends yielded equivalent fingerprints and attribution results, confirming

that the annual-mean value is sufficient. CO_2, CH_4, and O_3 trends were derived from the baseline datasets used to construct the hourly profiles.

Deriving multi-decadal liquid and ice cloud optical depth trends is complicated by temporal discontinuities of the MICROBASE record caused by instrument upgrades and outages. To circumvent this issue, the COD trend over the stable operational period of 2011–2014 is used instead. Because linearly extrapolating this short-term trend across the full 26-year period can yield unphysical extremes at discrete vertical levels, the COD perturbation was fractionally capped, to not exceed $\pm 50\%$ of the baseline optical depth at any given hour and vertical layer. This preserves the vertical structure of the observed cloud profiles to ensure realistic radiative responses (dR) are simulated. Furthermore, additional sensitivity tests were conducted using both the Shupe-Turner cloud microphysics dataset[54] and the satellite-based Clouds and the Earth's Radiant Energy System (CERES) record[13] (Extended Data Fig. 1a). To stress-test this methodology, we also evaluated the Microbase PI dataset (2002–2011). Despite this earlier record being non-continuous and subject to higher observational biases prior to the Ka-band ARM Zenith Radar (KAZR) deployment (M. Deng, pers. comm.), the spectral shape of the cloud fingerprint proved exceptionally robust (Extended Data Fig. 1b). The spectral fingerprints computed from all tested perturbation schemes have high cross-correlations ($r > 0.99$; Extended Data Fig. 1c).

Prior to optimal fingerprinting, the hourly fingerprints were aggregated into monthly means using a flux-weighted averaging scheme:

$$\bar{\mathbf{S}}_m = \frac{\sum_{h \in m} \mathbf{S}_h |\Delta F_h|}{\sum_{h \in m} |\Delta F_h|} \quad (2)$$

where $|\Delta F_h|$ is the absolute value of spectrally integrated radiance change for hour h within month m. This weighting suppresses numerical artefacts from hours with near-zero net flux changes (e.g., when thick low clouds like a black-body occur near the surface), ensuring that periods with distinct, high signal-to-noise radiative forcing dominate the temporal mean. Sensitivity tests replacing the hourly flux weights

$|\Delta F_h|$ with the monthly mean flux yielded the same spectral fingerprints, confirming that the choice of weighting scheme does not affect the results.

Optimal fingerprinting method

We attribute the observed DLR trend[24] ($\mathbf{\Delta R}$) to its drivers using the optimal fingerprinting framework of ref.[8]. In this framework, the trend $\mathbf{\Delta R}$ ($n_\nu \times 1$) is modelled as a linear combination of the fingerprints ($\mathbf{S}$, $n_\nu \times n_{var}$):

$$\mathbf{\Delta R} = \mathbf{S}\hat{\boldsymbol{a}} + \boldsymbol{r} \tag{3}$$

where n_ν is the number of spectral channels and n_{var}, the number of regression variables. Here, $\hat{\boldsymbol{a}}$ ($n_{var} \times 1$) is the vector of unknown scaling coefficients and $\boldsymbol{r}$ ($n_\nu \times 1$) the residual vector. The optimal estimate for $\hat{\boldsymbol{a}}$ minimizes the residual variance weighted by $\mathbf{C^{-1}}$, the inverse total uncertainty covariance:

$$\hat{\boldsymbol{a}} = (\mathbf{S}^T\mathbf{C}^{-1}\mathbf{S})^{-1}\mathbf{S}^T\boldsymbol{C}^{-1}\mathbf{\Delta R} \tag{4}$$

$\mathbf{C}$ ($n_\nu \times n_\nu$) combines observational ($\mathbf{C}_{nv}$, from ref.[24]), fingerprint ($\mathbf{C}_{fp}$), and non-linearity ($\mathbf{C}_{nl}$) uncertainty (Extended Data Fig. 11). To stabilize the inversion and avoid overfitting, we reconstruct $\mathbf{C}^{-1}$ from its first n_e eigenvectors (EOF truncation). n_e is chosen as the point where the residual RMS and the consistency ratio (χ^2/DOF, where χ^2 is the weighted residual sum of squares and DOF the degrees of freedom remaining after component fitting) jointly stabilize, leaving enough degrees of freedom to resolve all six components. Coefficient uncertainties are given by $\hat{\mathbf{C}}_\mathbf{a} = (\mathbf{S}^T\mathbf{C}^{-1}\mathbf{S})^{-1}$, the diagonal of which gives the 1σ statistical confidence intervals; the total uncertainties reported in Fig. 1 include an additional term arising from the FIR treatment as detailed below.

Far-Infrared Spectral Attribution

The spectral fingerprinting in the FIR water vapour rotation band (420–590 cm^{-1}) faces compounding problems. First, documented uncertainties in the FIR water vapour continuum[55–57], poorly constrained ice cloud radiative properties in the FIR[58–60], and limited observational constraints on Arctic moisture

profiles[61,62] and cloud microphysical properties[28,29] collectively degrade the spectral fingerprint accuracy in this band. Second, the spectral fingerprints of temperature, water vapour, and clouds are inter-correlated in this band—temperature is anti-correlated with both water vapour (r = -0.88) and clouds (r = -0.84), while water vapour and clouds correlate positively (r = 0.76)—compared to near-orthogonal relationship between them in the 590-1700 cm^{-1} range (r = 0.01, -0.19, and 0.56 respectively). These entangled spectral structures may lead to degeneracies in the inversion (Extended Data Fig. 3a, e). Finally, E-AERI measured radiance trends have lower signal-to-noise ratio (SNR) values in the FIR (Extended Data Fig. 3d), due to high natural atmospheric variability and to a lesser extent instrumental noise[24]. To mitigate these challenges, we screened the FIR radiance trends channel-by-channel based on the observational SNR, defined as $SNR(\nu) = |\Delta R(\nu)|/\sigma_{obs}(\nu)$, where $\sigma_{obs}(\nu)$, is the 1σ E-AERI trend uncertainty[24]. Channels within 420–590 cm^{-1} with an SNR below 1.5 were excluded from the regression, retaining the 109 channels that carry detectable signals, while all channels above 590 cm^{-1} were kept at full weight (Extended Data Fig. 3). The flux left unattributed by the discarded channels was propagated as a structural uncertainty: the residual between the observed trend and the fitted reconstruction, evaluated over the full 420–590 cm^{-1} band, was multiplied by $\kappa(\nu)$ and integrated (see Radiance-to-Flux conversion below) to yield a 1σ structural uncertainty term for the temperature, water vapour, and cloud components. The total 95% confidence interval for each affected component was then computed as $2\sqrt{\sigma_{stat}^2 + \sigma_{FIR}^2}$, where σ_{stat} is the 1σ statistical uncertainty derived from the GLS covariance matrix $(\mathbf{S}^T\mathbf{C}^{-1}\mathbf{S})^{-1}$, and σ_{FIR} is the 1σ FIR structural uncertainty. For components insensitive to the FIR (CO_2, CH_4, O_3), the total uncertainty reflects the statistical term alone, scaled to 95% as $2\sigma_{stat}$. We confirmed that the attribution is robust to this threshold choice: down-weighting low-signal channels via covariance inflation, rather than removing them outright, leaves the temperature and cloud attributions essentially unchanged (Extended Data Fig. 3b, c).

Radiance-to-Flux conversion

As E-AERI measures the DLR $R(\nu,\mu)$ from a single zenith viewing geometry ($\mu = cos\theta$), we derived a spectral conversion ratio, $\kappa(\nu)$, to convert it to angularly integrated irradiance flux $F(\nu)$. We define the relationship as:

$$F(\nu) = 2\pi \int_0^1 R(\nu,\mu)\mu d\mu = \kappa(\nu)R(\nu,\text{zenith}) \quad (5)$$

where $\kappa(\nu)$ acts as a correction factor that accounts for the angular anisotropy of the DLR field. Following the method established in ref.[63], we simulated the full angular radiance distribution using the DISORT model with 16 streams. The hemispheric flux $F(\nu)$ was determined via Gaussian quadrature integration over 5 nodes. Physically, $\kappa(\nu)$ accounts for the limb-darkening (or brightening) effect that occurs as the optical path length thickens toward the horizon, diverging from an isotropic value of π in semi-transparent spectral windows while converging to π within highly opaque, saturated absorption bands. The resulting yearly-averaged spectral κ coefficients are displayed in Extended Data Fig. 4.

Broadband radiometer trend

The broadband surface downwelling longwave trend at NSA was computed from the ARM QCRAD1LONG data product[38]. Quality-controlled 1-min downwelling longwave irradiances (retaining only samples flagged good by the QCRAD quality field) were averaged to monthly means over 2003–2023; the 12-month climatology was removed, and an ordinary-least-squares trend was fitted to the deseasonalized anomalies, with the reported 95% confidence interval derived from the regression slope standard error. The pyrgeometer trend of 6.22 ± 2.60 W m^{-2} per decade is found to be far less precise than the E-AERI estimate of 3.72 ± 0.74 W m^{-2} per decade, reflecting the larger month-to-month scatter of the broadband anomaly series. The magnitude difference between the two instruments is not an artefact of differing spectral integration windows: although the fingerprinting spans 10–2000 cm^{-1} versus the pyrgeometer's nominal ~200–2857 cm^{-1} (3.5–50 μm), the 2000–2857 cm^{-1} band contributes < 1% of the surface downwelling flux at Arctic temperatures, so the fingerprinting recovers the full longwave trend.

Data Availability

The E-AERI radiance, ARMBE, QCRAD1LONG and MICROBASE datasets are available from the ARM Data Discovery portal (https://adc.arm.gov). ERA5 reanalysis data are available from the Copernicus Climate Data Store (https://cds.climate.copernicus.eu/datasets). ERA5 radiative kernel data[32] used for independent validation are available via Mendeley Data (https://doi.org/10.17632/gpm9rvtnpr). MERRA-2 reanalysis data are available from the NASA Goddard Earth Sciences Data and Information Services Center (https://disc.gsfc.nasa.gov). CERES-EBAF data are available from the NASA Langley Research Center Atmospheric Science Data Center (https://ceres.larc.nasa.gov/data/). CarbonTracker data and NOAA Global Monitoring Laboratory atmospheric trace gas measurements are available from https://gml.noaa.gov. The Shupe-Turner cloud microphysics dataset is available from the NOAA Physical Sciences Laboratory (https://psl.noaa.gov). CMIP6 model output is available via the Earth System Grid Federation (https://esgf-node.llnl.gov).

Code Availability

Code used to perform the spectral fingerprinting decomposition and generate the figures in this study will be made available as a Code Ocean compute capsule upon peer review, with a DOI issued on publication.

References

1. Cohen, J. *et al.* Recent Arctic amplification and extreme mid-latitude weather. *Nature Geosci* **7**, 627–637 (2014).
2. Taylor, P. C. *et al.* Process Drivers, Inter-Model Spread, and the Path Forward: A Review of Amplified Arctic Warming. *Front. Earth Sci.* **9**, 758361 (2022).
3. Huang, Y., Leroy, S., Gero, P. J., Dykema, J. & Anderson, J. Separation of longwave climate feedbacks from spectral observations. *J. Geophys. Res.* **115**, 2009JD012766 (2010).
4. Feldman, D. R. *et al.* Observational determination of surface radiative forcing by CO2 from 2000 to 2010. *Nature* **519**, 339–343 (2015).

5. Hasselmann, K. Multi-pattern fingerprint method for detection and attribution of climate change. *Climate Dynamics* **13**, 601–611 (1997).
6. Leroy, S., Anderson, J., Dykema, J. & Goody, R. Testing Climate Models Using Thermal Infrared Spectra. *Journal of Climate* **21**, 1863–1875 (2008).
7. Huang, Y., Leroy, S. S. & Anderson, J. G. Determining Longwave Forcing and Feedback Using Infrared Spectra and GNSS Radio Occultation. *Journal of Climate* **23**, 6027–6035 (2010).
8. Liu, L., Huang, Y. & Gyakum, J. R. Clouds reduce downwelling longwave radiation over land in a warming climate. *Nature* **637**, 868–874 (2025).
9. Pithan, F. & Mauritsen, T. Arctic amplification dominated by temperature feedbacks in contemporary climate models. *Nature Geosci* **7**, 181–184 (2014).
10. Zelinka, M. D. *et al.* Causes of Higher Climate Sensitivity in CMIP6 Models. *Geophysical Research Letters* **47**, e2019GL085782 (2020).
11. Ceppi, P., Brient, F., Zelinka, M. D. & Hartmann, D. L. Cloud feedback mechanisms and their representation in global climate models. *WIREs Climate Change* **8**, e465 (2017).
12. Dong, X. *et al.* A 10 year climatology of Arctic cloud fraction and radiative forcing at Barrow, Alaska. *J. Geophys. Res.* **115**, 2009JD013489 (2010).
13. Kato, S. *et al.* Surface Irradiances of Edition 4.0 Clouds and the Earth's Radiant Energy System (CERES) Energy Balanced and Filled (EBAF) Data Product. *Journal of Climate* **31**, 4501–4527 (2018).
14. L'Ecuyer, T. S. *et al.* The Polar Radiant Energy in the Far Infrared Experiment: A New Perspective on Polar Longwave Energy Exchanges. *Bulletin of the American Meteorological Society* **102**, E1431–E1449 (2021).
15. Palchetti, L. *et al.* FORUM: Unique Far-Infrared Satellite Observations to Better Understand How Earth Radiates Energy to Space. *Bulletin of the American Meteorological Society* **101**, E2030–E2046 (2020).

16. Langille, J. *et al.* The High-Altitude Aerosols, Water Vapor, and Clouds Mission: Concept, Scientific Objectives, and Data Products. *Bulletin of the American Meteorological Society* **106**, E2358–E2383 (2025).

17. Bertossa, C. & L'Ecuyer, T. A Rapid Deterioration of the Transmissive Atmospheric Radiative Regime in the Western Arctic. *Geophysical Research Letters* **52**, e2025GL115362 (2025).

18. Bertrand, L., Kay, J. E. & De Boer, G. Increasing wintertime cloud opacity increases surface longwave radiation at a long-term Arctic observatory. *Nat Commun* **16**, 9135 (2025).

19. Cox, C. J. *et al.* The De-Icing Comparison Experiment (D-ICE): a study of broadband radiometric measurements under icing conditions in the Arctic. *Atmos. Meas. Tech.* **14**, 1205–1224 (2021).

20. Philipona, R. *et al.* Atmospheric longwave irradiance uncertainty: Pyrgeometers compared to an absolute sky-scanning radiometer, atmospheric emitted radiance interferometer, and radiative transfer model calculations. *J. Geophys. Res.* **106**, 28129–28141 (2001).

21. Knuteson, R. O. *et al.* Atmospheric Emitted Radiance Interferometer. Part I: Instrument Design. *Journal of Atmospheric and Oceanic Technology* **21**, 1763–1776 (2004).

22. Knuteson, R. O. *et al.* Atmospheric Emitted Radiance Interferometer. Part II: Instrument Performance. *Journal of Atmospheric and Oceanic Technology* **21**, 1777–1789 (2004).

23. Gero, J., Hackel, D. & Garcia, R. Atmospheric Emitted Radiance Interferometer (AERI) Handbook. 1 GB Atmospheric Radiation Measurement (ARM) Archive, Oak Ridge National Laboratory (ORNL), Oak Ridge, TN (US); https://doi.org/10.5439/1253918 (2005).

24. Riot-Bretêcher, B., Huang, Y., Liu, L. & Gero, J. Strengthening Atmospheric Greenhouse Effect at the Arctic North Slope of Alaska Site Evidenced by Long-Term Records of the Downwelling Longwave Radiance Spectrum. *JGR Atmospheres* **130**, e2025JD043680 (2025).

25. Morrison, H. *et al.* Resilience of persistent Arctic mixed-phase clouds. *Nature Geosci* **5**, 11–17 (2012).

26. Shupe, M. D. & Intrieri, J. M. Cloud Radiative Forcing of the Arctic Surface: The Influence of Cloud Properties, Surface Albedo, and Solar Zenith Angle. *J. Climate* **17**, 616–628 (2004).

27. Liu, L., Huang, Y., Gyakum, J. R., Turner, D. D. & Gero, P. J. Trends in Downwelling Longwave Radiance Over the Southern Great Plains. *JGR Atmospheres* **127**, e2021JD035949 (2022).

28. Zhao, C. *et al.* Toward understanding of differences in current cloud retrievals of ARM ground-based measurements. *J. Geophys. Res.* **117**, 2011JD016792 (2012).

29. Zhao, C., Xie, S., Chen, X., Jensen, M. P. & Dunn, M. Quantifying uncertainties of cloud microphysical property retrievals with a perturbation method. *JGR Atmospheres* **119**, 5375–5385 (2014).

30. Goosse, H. *et al.* Quantifying climate feedbacks in polar regions. *Nat Commun* **9**, 1919 (2018).

31. Huang, H. & Huang, Y. Radiative sensitivity quantified by a new set of radiation flux kernels based on the ECMWF Reanalysis v5 (ERA5). *Earth Syst. Sci. Data* **15**, 3001–3021 (2023).

32. Huang, H., Huang, Y., Wei, Q. & Hu, Y. Band-by-band spectral radiative kernels based on the ERA5 reanalysis. *Sci Data* **11**, 237 (2024).

33. Mülmenstädt, J., Lubin, D., Russell, L. M. & Vogelmann, A. M. Cloud Properties over the North Slope of Alaska: Identifying the Prevailing Meteorological Regimes. *Journal of Climate* **25**, 8238–8258 (2012).

34. Hersbach, H. *et al.* The ERA5 global reanalysis. *Quart J Royal Meteoro Soc* **146**, 1999–2049 (2020).

35. Copernicus Climate Change Service. ERA5 monthly averaged data on single levels from 1940 to present. Copernicus Climate Change Service (C3S) Climate Data Store (CDS) https://doi.org/10.24381/CDS.F17050D7 (2019).

36. Eyring, V. *et al.* Overview of the Coupled Model Intercomparison Project Phase 6 (CMIP6) experimental design and organization. *Geosci. Model Dev.* **9**, 1937–1958 (2016).

37. Cesana, G., Kay, J. E., Chepfer, H., English, J. M. & De Boer, G. Ubiquitous low-level liquid-containing Arctic clouds: New observations and climate model constraints from CALIPSO-GOCCP. *Geophysical Research Letters* **39**, 2012GL053385 (2012).

38. Long, C. & Shi, Y. *The QCRad Value Added Product: Surface Radiation Measurement Quality Control Testing, Including Climatology Configurable Limits*. DOE/SC-ARM/TR-074, 1019540 http://www.osti.gov/servlets/purl/1019540-wnRFfU/ (2006) doi:10.2172/1019540.

39. Chen, X. & Xie, S. armbeatm. Atmospheric Radiation Measurement (ARM) Archive, Oak Ridge National Laboratory (ORNL), Oak Ridge, TN (US); ARM Data Center, Oak Ridge National Laboratory (ORNL), Oak Ridge, TN (United States) https://doi.org/10.5439/1333748 (1994).

40. Copernicus Climate Change Service. ERA5 hourly data on pressure levels from 1940 to present. Copernicus Climate Change Service (C3S) Climate Data Store (CDS) https://doi.org/10.24381/CDS.BD0915C6 (2018).

41. Serreze, M. C. & Barry, R. G. Processes and impacts of Arctic amplification: A research synthesis. *Global and Planetary Change* **77**, 85–96 (2011).

42. Wielicki, B. A. *et al.* Achieving Climate Change Absolute Accuracy in Orbit. *Bulletin of the American Meteorological Society* **94**, 1519–1539 (2013).

43. Wetherald, R. T. & Manabe, S. Cloud Feedback Processes in a General Circulation Model. *J. Atmos. Sci.* **45**, 1397–1416 (1988).

44. Clough, S. A. *et al.* Atmospheric radiative transfer modeling: a summary of the AER codes. *Journal of Quantitative Spectroscopy and Radiative Transfer* **91**, 233–244 (2005).

45. Stamnes, K., Tsay, S.-C., Wiscombe, W. & Jayaweera, K. Numerically stable algorithm for discrete-ordinate-method radiative transfer in multiple scattering and emitting layered media. *Appl. Opt.* **27**, 2502 (1988).

46. Global Modeling and Assimilation Office & Pawson, S. MERRA-2 inst3_3d_chm_Nv: 3d,3-Hourly,Instantaneous,Model-Level,Assimilation,Carbon Monoxide and Ozone Mixing Ratio V5.12.4. NASA Goddard Earth Sciences Data and Information Services Center https://doi.org/10.5067/HO9OVZWF3KW2 (2015).

47. Jacobson, A. R. *et al.* CarbonTracker CT2025. Preprint at https://doi.org/10.15138/V4W1-2085 (2025).

48. NOAA ESRL GML CCGG Group. Earth System Research Laboratory Carbon Cycle and Greenhouse Gases Group Flask-Air Sample Measurements of CO2 at Global and Regional Background Sites, 1967-Present. NOAA ESRL GML CCGG Group https://doi.org/10.15138/WKGJ-F215 (2019).

49. NOAA ESRL GML CCGG Group. Earth System Research Laboratory Carbon Cycle and Greenhouse Gases Group Flask-Air Sample Measurements of CH4 at Global and Regional Background Sites, 1967-Present. NOAA ESRL GML CCGG Group https://doi.org/10.15138/VNCZ-M766 (2019).

50. Elkins, J. W., Nance, D. & Hall, B. Earth System Research Laboratory Halocarbons and Other Atmospheric Trace Gases Chromatograph for Atmospheric Trace Species (CATS) Measurements. NOAA National Centers for Environmental Information https://doi.org/10.7289/V5X0659V (2017).

51. Feng, J., Menzel, R. & Paynter, D. Toward Transparency and Consistency: An Open-Source Optics Parameterization for Clouds and Precipitation. *J Adv Model Earth Syst* **17**, e2024MS004478 (2025).

52. Yang, P. *et al.* Spectrally Consistent Scattering, Absorption, and Polarization Properties of Atmospheric Ice Crystals at Wavelengths from 0.2 to 100 μm. *Journal of the Atmospheric Sciences* **70**, 330–347 (2013).

53. USDOE Office of Science (SC), Biological and Environmental Research (BER) *et al. Continuous Baseline Microphysical Retrieval (MICROBASE) Value-Added Product Report*. DOE/SC-ARM-TR--095, 3003141 https://www.osti.gov/biblio/3003141 (2025) doi:10.2172/3003141.

54. Shupe, M. D. *et al.* Deriving Arctic Cloud Microphysics at Barrow, Alaska: Algorithms, Results, and Radiative Closure. *Journal of Applied Meteorology and Climatology* **54**, 1675–1689 (2015).

55. Turner, D. D. & Mlawer, E. J. The Radiative Heating in Underexplored Bands Campaigns. *Bull. Amer. Meteor. Soc.* **91**, 911–924 (2010).

56. Mlawer, E. J. *et al.* Analysis of Water Vapor Absorption in the Far-Infrared and Submillimeter Regions Using Surface Radiometric Measurements From Extremely Dry Locations. *JGR Atmospheres* **124**, 8134–8160 (2019).

57. Palchetti, L., Bianchini, G., Di Natale, G. & Del Guasta, M. Far-Infrared Radiative Properties of Water Vapor and Clouds in Antarctica. *Bulletin of the American Meteorological Society* **96**, 1505–1518 (2015).

58. Yang, P. *et al.* Spectral signature of ice clouds in the far-infrared region: Single-scattering calculations and radiative sensitivity study. *J. Geophys. Res.* **108**, 2002JD003291 (2003).

59. Libois, Q. *et al.* A microbolometer-based far infrared radiometer to study thin ice clouds in the Arctic. *Atmos. Meas. Tech.* **9**, 1817–1832 (2016).

60. Libois, Q. & Blanchet, J. Added value of far-infrared radiometry for remote sensing of ice clouds. *JGR Atmospheres* **122**, 6541–6564 (2017).

61. Walbröl, A. *et al.* Moisture inversions in the central Arctic: Product assessment and long-wave radiative effect. *Quart J Royal Meteoro Soc* **152**, e70110 (2026).

62. Mosselmans, S. *et al.* Exploring Clear-Sky Longwave Radiative Closure in the Arctic: A Downwelling Case Study. *Atmospheric Science Letters* **27**, e70000 (2026).

63. Li, J. Gaussian Quadrature and Its Application to Infrared Radiation. *J. Atmos. Sci.* **57**, 753–765 (2000).

64. Global Modeling and Assimilation Office & Pawson, S. MERRA-2 tavgM_2d_rad_Nx: 2d,Monthly mean,Time-Averaged,Single-Level,Assimilation,Radiation Diagnostics V5.12.4. NASA Goddard Earth Sciences Data and Information Services Center https://doi.org/10.5067/OU3HJDS973O0 (2015).

Acknowledgements

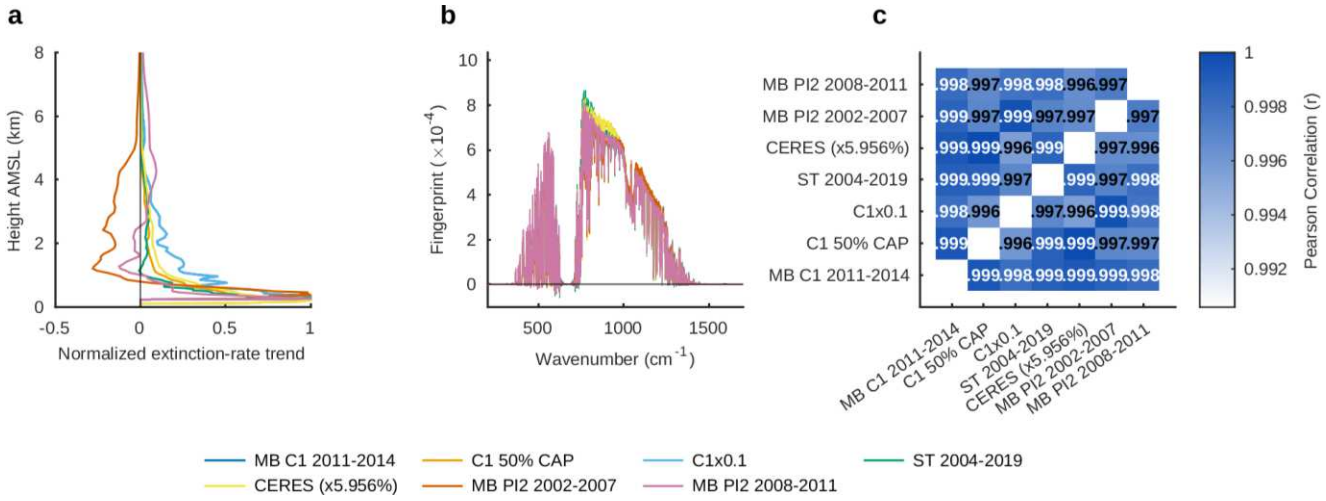
We thank L. Liu, H. Huang and other members of the Atmospheric Radiation Group at McGill University for discussions and comments on this work. We acknowledge the funding from Natural Sciences and Engineering Research Council of Canada (RGPIN‐2025‐05397) and Environment and Climate Change Canada (EDF‐CA‐2021i022). We also acknowledge the support of the Digital Research Alliance of Canada and Calcul Québec for providing access to the Rorqual supercomputer used in this research.

Ethics declarations

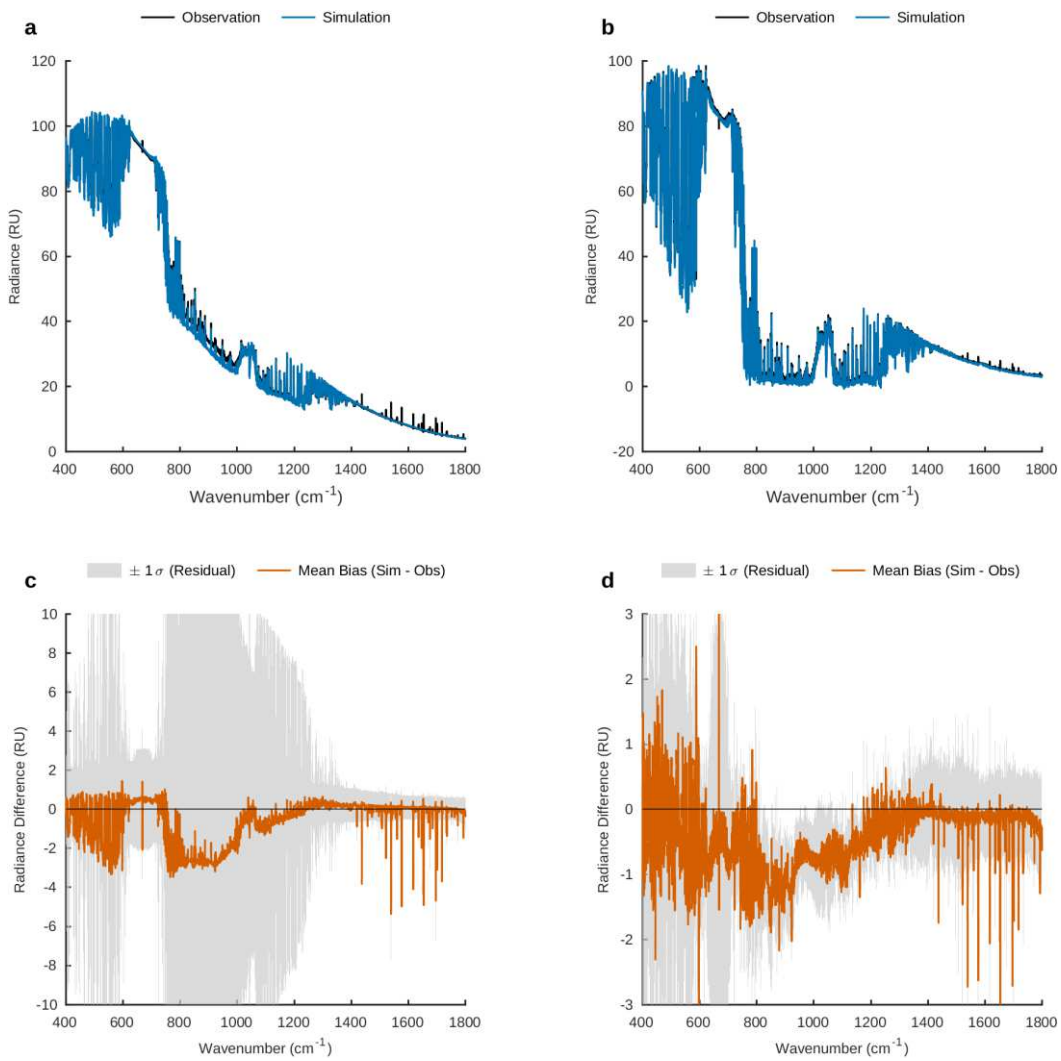
Competing interests

The authors declare no competing interests.

Supplementary Information

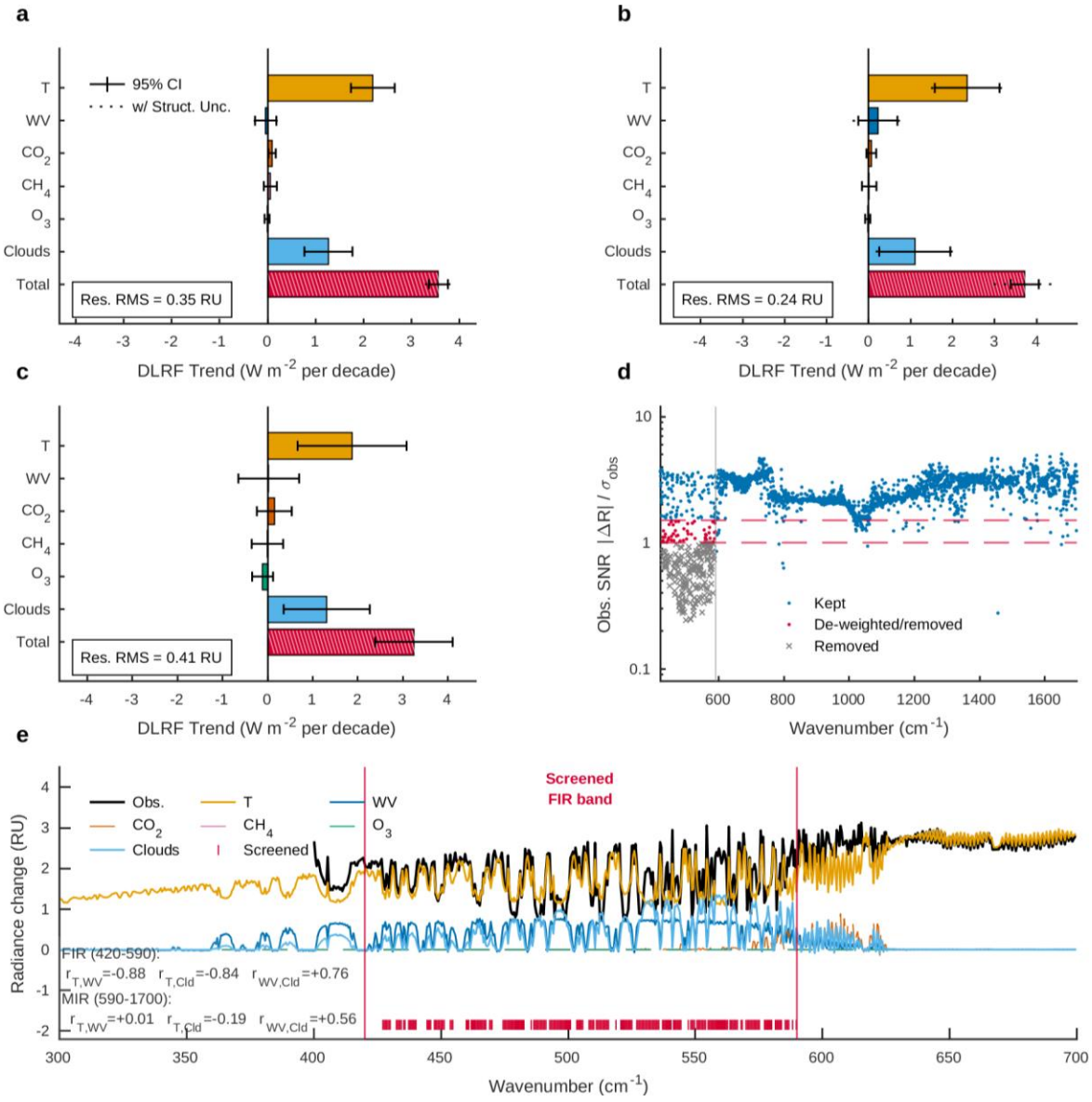


Extended Data Fig. 1: Robustness of the cloud spectral fingerprint across optical depth perturbation schemes. a, Normalized total (liquid+ice) cloud extinction coefficient trend profiles from multiple independent datasets—Microbase (MB) PI2, Microbase, Shupe-Turner (ST), and CERES—and under varied perturbation constraints. Tested constraints include fractional capping of the layer-maximum optical depth change (50%), and applying a fixed 5.956% optical depth increase, derived from the 26-year CERES visible optical depth trend. The perturbation was applied at a given level only where cloud particles of that phase were present. Notably, applying the perturbation uniformly across all times and vertical levels yielded negligible changes to the resulting fingerprints. **b,** Corresponding normalized cloud spectral fingerprints **c,** Pearson cross-correlation matrix (r) comparing the resulting spectral morphologies; all pairwise correlations exceed $r = 0.99$. The consistently high cross-correlation demonstrates that the shape of the cloud fingerprint is a physically intrinsic signature, remaining invariant regardless of the underlying observational dataset or the magnitude of the applied perturbation.



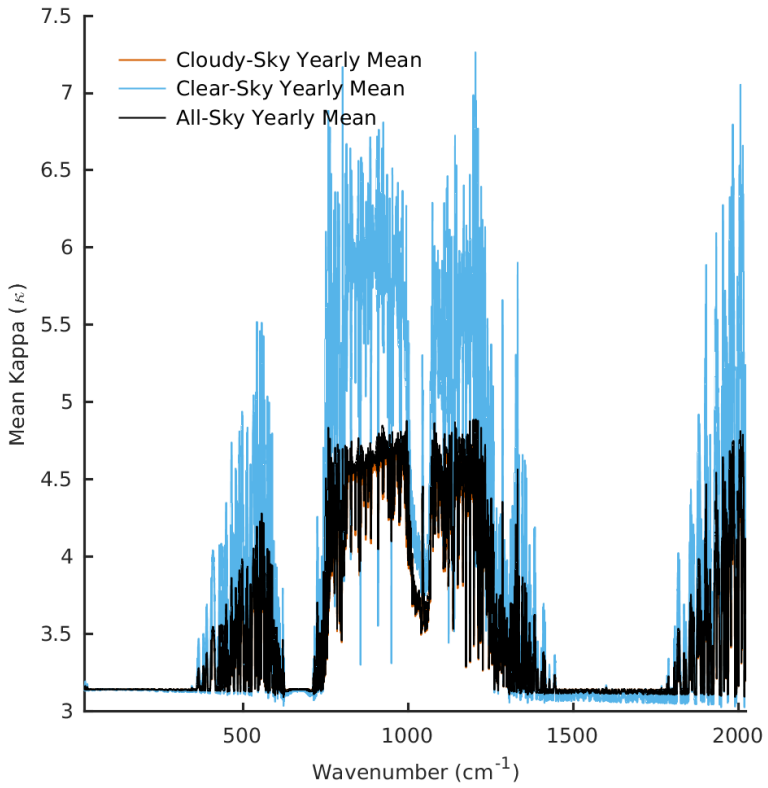
604 **Extended Data Fig. 2: Radiative closure between E-AERI observations and LBLRTM/DISORT**
605 **simulations. a**, Comparison of mean all-sky DLR spectra between E-AERI observations (black) and
606 LBLRTM/DISORT simulations (blue) for 2003. **b**, Same as **a**, but for clear-sky conditions. **c**, **d**, Radiance
607 difference (simulation minus observation) and the associated 1σ residual uncertainty (shaded) for all-sky
608 and clear-sky conditions, respectively. The mean bias (orange) indicates systematic model performance,
609 while the residual spread quantifies the representation error inherent in the hourly comparison. These
610 results confirm the model's high fidelity in capturing the spectral variability of Arctic DLR. The 2013
611 residuals exhibited a similar order of magnitude.

612

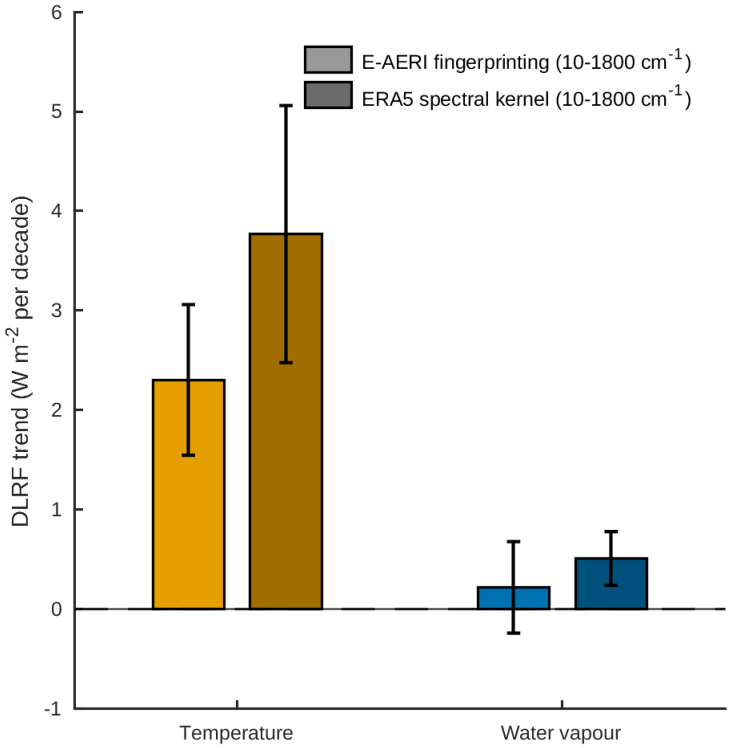


613 **Extended Data Fig. 3: Far-infrared signal-to-noise screening and attribution robustness. a,**
614 Attribution of decadal DLRF trends when the full FIR rotation band (420–590 cm^{-1}) is included without
615 screening. The water vapour attribution is statistically indeterminate due to spectral degeneracy, and the
616 residual RMS is elevated (0.35 RU). **b,** Attribution using the primary channel-by-channel signal-to-noise
617 ratio (SNR) screen, which removes noise-dominated FIR channels (SNR < 1.5). This resolves the
618 degeneracy, yielding physically consistent results and improving the fit quality (residual RMS = 0.24
619 RU); among the 109 retained channels, the inter-fingerprint FIR correlations fall to r = -0.55 (T-WV), -
620 0.46 (T-cloud), and +0.53 (WV-cloud), compared to the full-band values in **e**. **c,** Robustness check where
621 low-SNR FIR channels are de-weighted via covariance inflation rather than removed. The attribution of
622 the dominant components (Temperature and Clouds) is statistically identical to **b,** confirming that the
623 results are insensitive to the specific FIR treatment. For **a–c**, solid error bars represent the 95% statistical

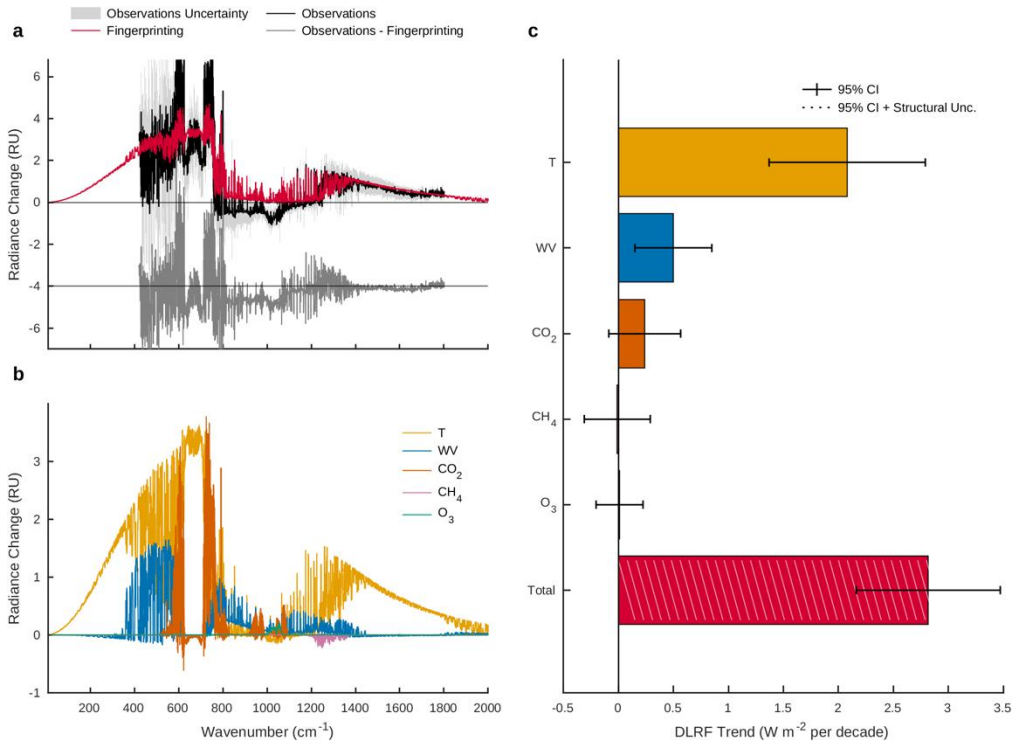
confidence interval; dotted extensions indicate the total uncertainty including the structural penalty from unattributed FIR flux. **d,** Observational signal-to-noise ratio of the E-AERI 26-year radiance trend at each spectral channel across the 420–1700 cm^{-1} analysis band. The screen is applied only within the FIR rotation band (420–590 cm^{-1}; grey vertical line marks the 590 cm^{-1} edge): channels there with SNR below the threshold (red dashed line) are excluded from the primary optimization (grey crosses), while those above it are retained (blue dots). De-weighted channels (SNR between 1 and 1.5) are shown as red dots. All channels above 590 cm^{-1} are kept at full weight regardless of SNR. The FIR is systematically the lowest-SNR region of the spectrum, motivating the channel-by-channel screen described in Methods. **e,** Scaled spectral fingerprints of the primary atmospheric drivers compared with the observed 26-year E-AERI radiance trend. The specific FIR channels screened out in **b** are indicated by red vertical ticks along the baseline. The high collinearity between T, WV, and Clouds in the FIR (e.g., r = -0.88 between T and WV) illustrates the sign degeneracy that necessitates the SNR screen, in stark contrast to their near-orthogonality in the primary window (>590 cm^{-1}).



Extended Data Fig. 4: Spectrally resolved radiance-to-flux conversion factor (κ) across different sky conditions. Annual mean spectral distribution of the conversion ratio, κ, simulated across the infrared spectrum (10–2000 cm^{-1}) for clear-sky (blue line), cloudy-sky (orange line), and all-sky (black line) conditions.

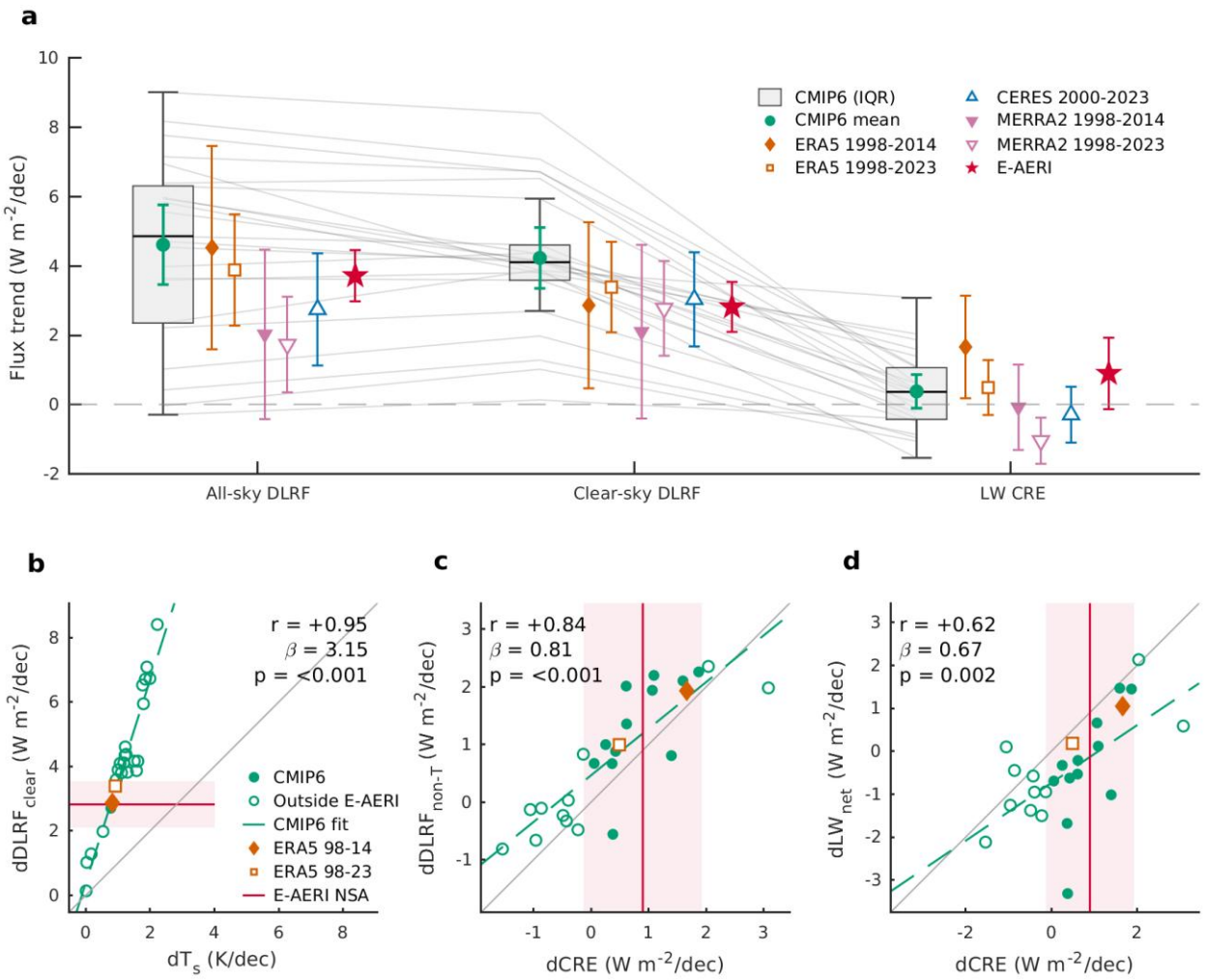


643 **Extended Data Fig. 5: Independent validation of temperature and water vapour DLRF trends using**
644 **ERA5 radiative kernels.** Comparison of decadal temperature and water vapour all-sky contributions to
645 the surface DLRF trend at NSA, derived from two independent methods: E-AERI optimal spectral
646 fingerprinting (light blue/yellow, 10–1800 cm^{-1}) and ERA5 RRTM radiative kernels[31,32] applied to ERA5
647 reanalysis anomalies over 1998–2023 (dark blue/yellow, spectral sum over 10–1800 cm^{-1}). Error bars
648 represent 95% confidence intervals, combining trend detection uncertainty and kernel representativeness
649 uncertainty (temporal inter-annual variability and spatial variability across a ±2.5° region) propagated in
650 quadrature.
651



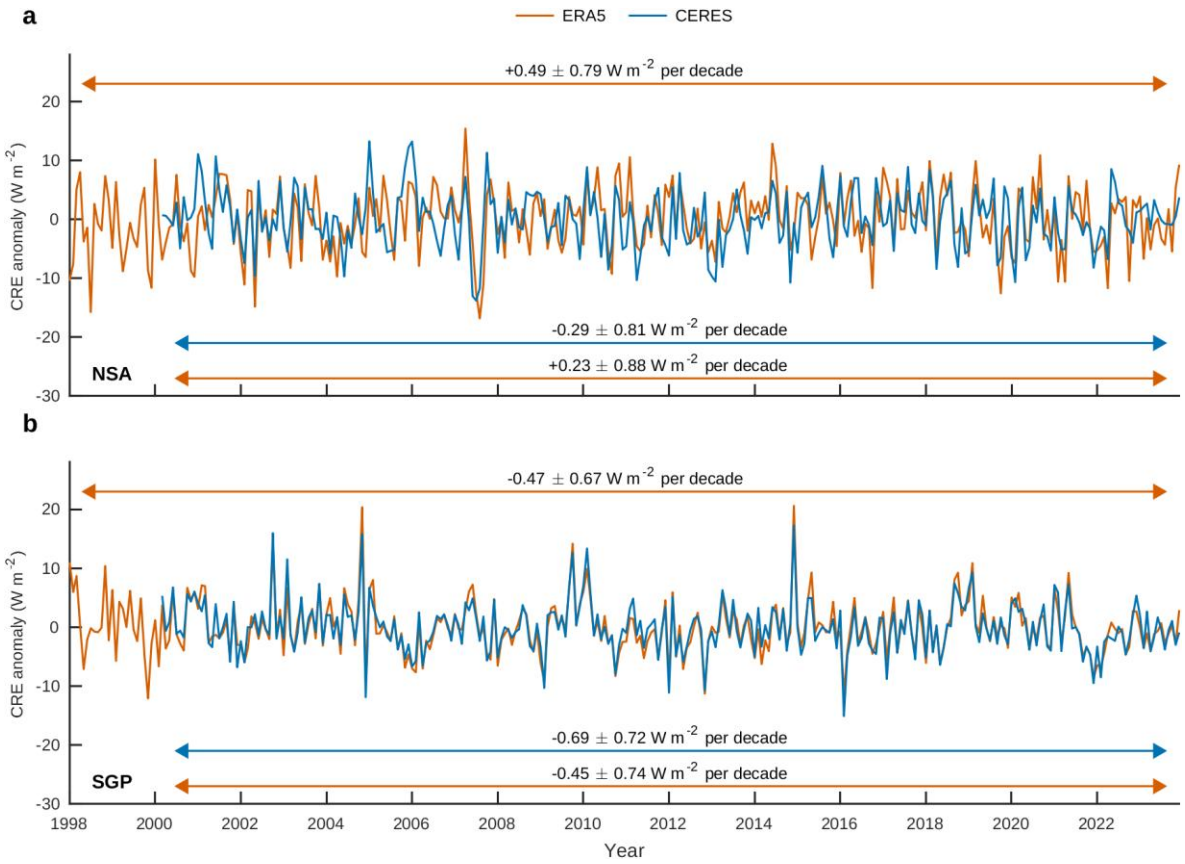
652 **Extended Data Fig. 6: Clear-sky spectral attribution at NSA. a,** Observed 26-year E-AERI clear-sky
653 radiance trend (black) with its 1σ observational uncertainty (grey shading), the optimal-fingerprinting
654 reconstruction (red), and the fit residual (grey, offset by -4 RU for clarity). **b,** Scaled spectral
655 contributions of the individual drivers: temperature (T), water vapour (WV), CO_2, CH_4, and O_3 obtained
656 by multiplying each normalized clear-sky fingerprint by its retrieved scaling factor. **c,** Component-
657 resolved decadal clear-sky DLRF trends from converting the spectral attributions in **b** to broadband flux
658 via the $\kappa_{clr}(\nu)$ radiance-to-flux factor (see Methods), with the total at bottom. Error bars are 95%
659 confidence intervals from the GLS regression; the full infrared band (420–1700 cm^{-1}) is retained at full
660 weight, so no FIR signal-to-noise screen or structural-uncertainty penalty is applied here. The total
661 uncertainty is propagated through the full parameter covariance matrix.

662



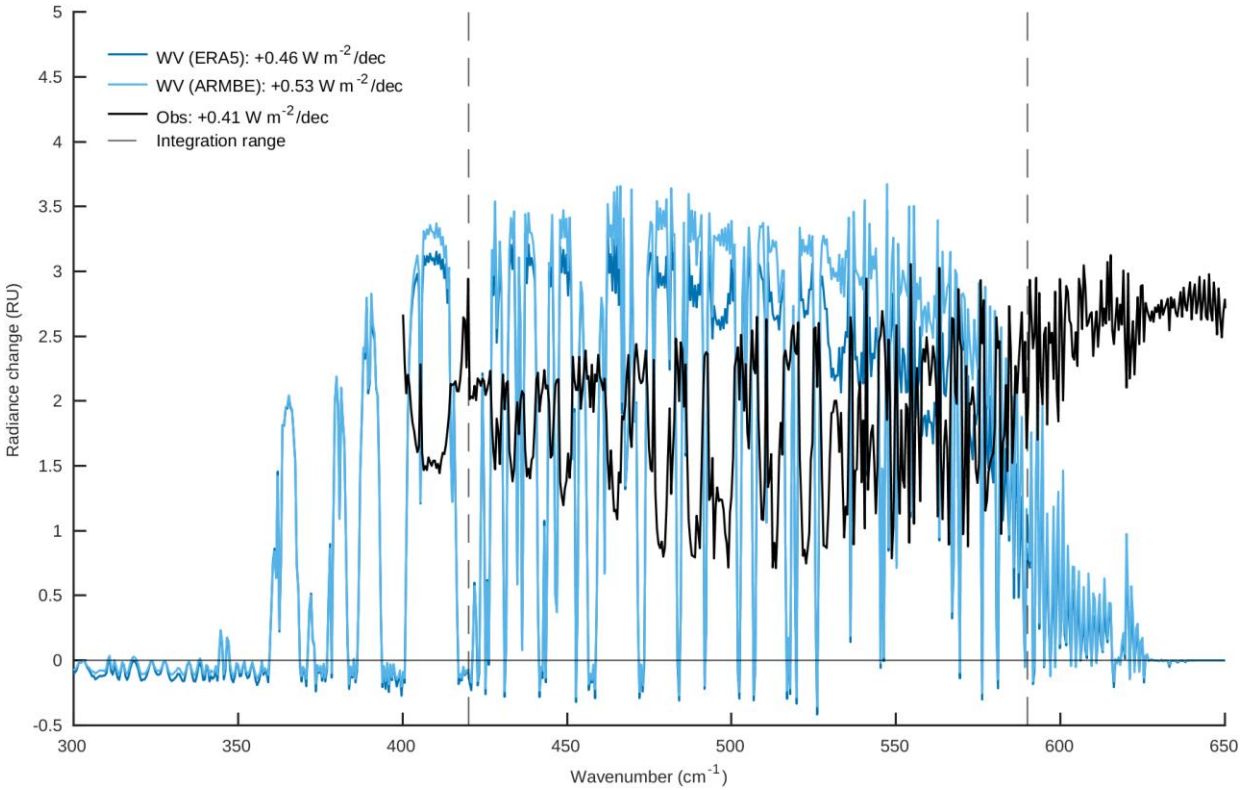
Extended Data Fig. 7: Surface longwave radiation trends at NSA and the spread that discriminates them. a, Decadal trends in all-sky DLRF, clear-sky DLRF, and LW CRE over a $\pm$ 2.5° latitude–longitude region centred on the NSA site. Trends are evaluated over 1998–2014 for the 23-model CMIP6 historical ensemble (faint grey lines, individual models; grey interquartile boxes with whiskers extending to 1.5x the interquartile range; green markers, ensemble mean; Extended Data Table 2). ERA5 (orange diamonds/squares), MERRA-2 (filled/open pink triangles) and CERES (open blue triangles) trends span 1998–2014 (filled) and 1998–2023 (open), with CERES over 2000–2023. E-AERI trends (red stars) are from optimal-fingerprinting over the 26-year record. Confidence intervals are 95%. **b–d**, Across the CMIP6 ensemble, relationships isolating the cloud signal from the temperature response: **b,** clear-sky DLRF trend versus surface-warming rate dT_s; **c,** the non-temperature component of the all-sky DLRF trend (all-sky minus the temperature-expected part, $\beta \times dT_s$) versus the LW CRE trend; **d,** the surface net-LW trend versus the LW CRE trend. Green points are individual models with a least-squares fit (dashed); inset *r*, β and *p-value*. Filled green points denote models whose clear-sky DLRF trend (**b**) or LW CRE trend (**c**, **d**) falls within the E-AERI 95% confidence interval (shaded); open points denote

models falling outside it. Orange markers in **b** and **c** show ERA5; the red line marks the E-AERI value with its 95% confidence interval (shaded). CERES surface fluxes are modelled from top-of-atmosphere observations, not directly measured[13]. Across the ensemble, clear-sky DLRF is set by the warming rate (**b**), the non-temperature DLRF tracks the CRE trend (**c**) and the CRE governs part of the net surface-LW trend (**d**); the E-AERI CRE constraint (red) excludes the most strongly negative models.

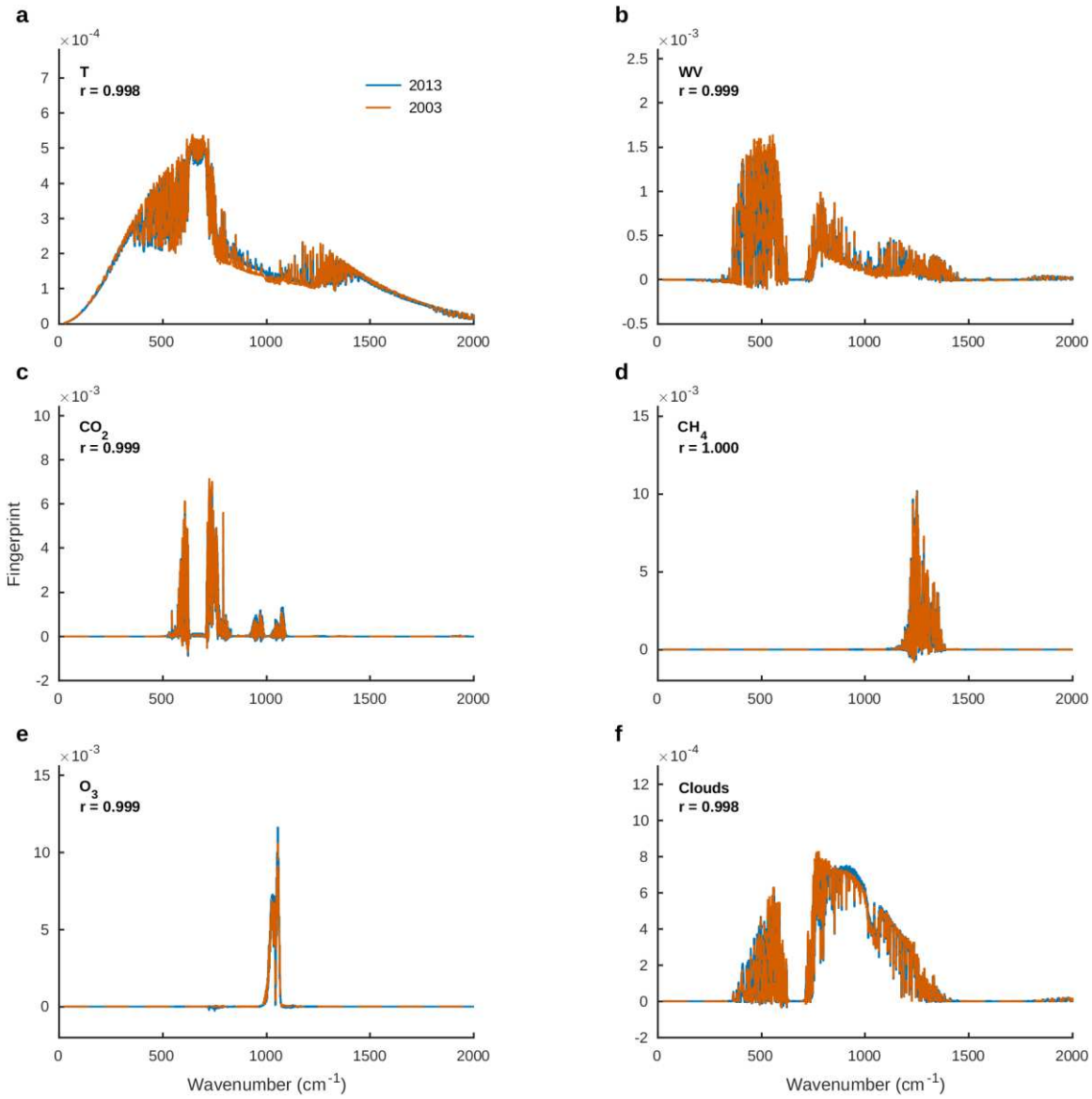


Extended Data Fig. 8: Monthly surface longwave CRE anomalies from ERA5 and CERES-EBAF at the NSA and SGP sites. Time series of monthly-mean surface downwelling longwave CRE anomalies (all-sky minus clear-sky downwelling longwave irradiance at the surface) for **a**, the NSA site (71.32° N, 156.62° W) and **b**, the SGP site (36.61° N, 97.49° W). Values are averaged over a ±2.5° latitude–longitude box centred on each site. Orange, ERA5 reanalysis; blue, CERES-EBAF Ed4.2.1. Anomalies are computed relative to the monthly-mean climatology of each dataset. Horizontal arrows indicate the periods over which linear trends are evaluated, with the corresponding trend ± 95% confidence interval (ordinary least-squares regression) annotated above each arrow. In each panel the upper (orange) arrow gives the ERA5 trend over its full record (1998–2023); the lower two arrows give the CERES and ERA5 trends over the common 2000–2023 period. These time series highlight that product disagreement is specific to the Arctic. At the mid-latitude SGP site, ERA5 and CERES agree closely in both interannual

693 variability and the sign and magnitude of the trend[8]. Conversely, at the NSA site, their anomaly time
694 series are only weakly correlated, and their trends disagree in sign. CERES-EBAF surface fluxes are
695 derived by radiative transfer modelling constrained by top-of-atmosphere observations[13], which
696 contributes to this divergence in the data-sparse Arctic. MERRA-2[64] further reinforces this disagreement,
697 demonstrating a lack of consensus at NSA (Extended Data Fig. 7).

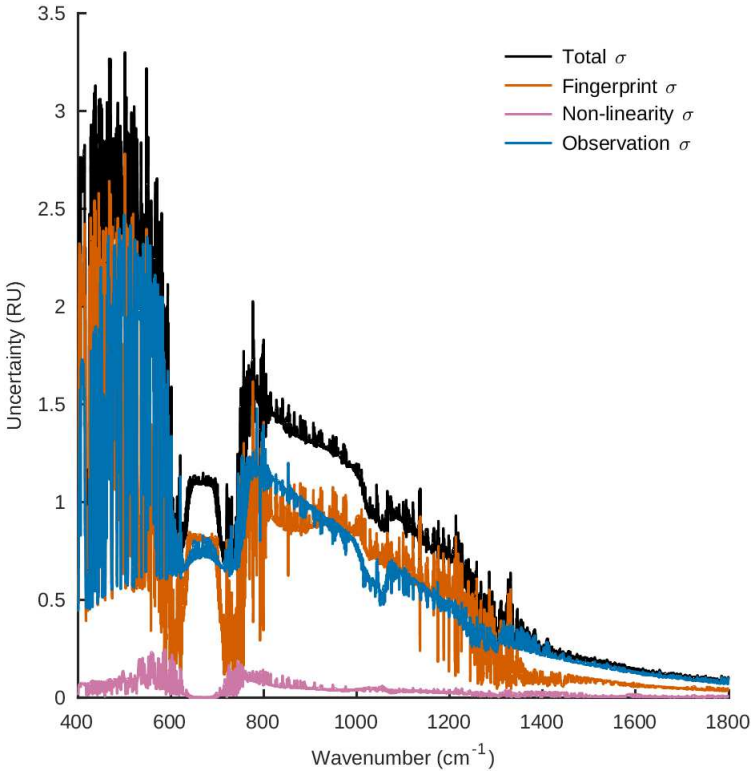


Extended Data Fig. 9: The FIR water-vapour response implied by reanalysis and observational humidity. Spectral radiance change across the far-infrared rotation band, comparing the observed E-AERI all-sky trend (blue) with the water-vapour-only response computed by the PRP method for two prescribed humidity trends: ERA5 (dark blue, derived from monthly-mean anomalies) and ARMBE (light blue, derived from seasonal-mean anomalies, used for the attribution). Dashed vertical lines mark the 420–590 cm^{-1} integration window. Legend values give the far-infrared flux trend (W m^{-2} per decade) obtained by integrating each radiance change over this window with the per-channel radiance-to-flux conversion $\kappa(\nu)$. The water vapour-only flux trend implied by both humidity products exceeds the total observed FIR trend, indicating that the prescribed moistening is too strong to be consistent with the spectrally resolved E-AERI record. The negative peaks reflect near-surface temperature inversions, which shift the effective downwelling emission level to a colder layer as prescribed humidity increases. The observed trend is also anti-correlated to the water vapour and cloud signals (Extended Data Fig. 3e), suggesting it is atmospheric warming, rather than moistening, that drives the FIR trend.



712 **Extended Data Fig. 10: Independence of spectral fingerprints from the reference climatology.**
713 Comparison of the spectral fingerprints derived using atmospheric profiles from two independent, neutral
714 reference years: 2003 (orange dashed lines) and 2013 (blue solid lines). Panels display the component-
715 specific fingerprints for **a**, Temperature; **b**, water vapour; **c**, CO_2; **d**, CH_4; **e**, O_3; and **f**, clouds.

716



Extended Data Fig. 11: Uncertainty budget for the all-sky optimal fingerprinting framework. The total uncertainty (σ_{tot}, black) and its components—internal fingerprint variability (σ_{fp}, orange), model non-linearity (σ_{nl}, pink), and observation (σ_{nv}, blue)—are represented by the square root of the diagonal components of their respective covariance matrices.

Extended Data Table 1. Fingerprinted decadal DLRF trends by component at NSA under all-sky and clear-sky conditions (1998–2023).

Component	All-sky DLRF trend (W m^{-2} dec^{-1})	Clear-sky DLRF trend (W m^{-2} dec^{-1})
Temperature	2.35 ± 0.86	2.08 ± 0.71
Water vapour	0.22 ± 0.60	0.50 ± 0.35
CO_2	0.06 ± 0.12	0.24 ± 0.33
CH_4	0.01 ± 0.17	-0.01 ± 0.30
O_3	-0.02 ± 0.06	0.01 ± 0.21
Clouds	1.10 ± 0.93	—
Total	**3.72 ± 0.74**	**2.82 ± 0.66**

All-sky uncertainties are 95% confidence intervals combining statistical uncertainty and the structural penalty from unattributed FIR flux (see Methods). Clear-sky uncertainties reflect statistical uncertainty only.

Extended Data Table 2. CMIP6 Historical trends in surface downwelling longwave radiation flux over the ±2.5° region surrounding NSA (1998–2014).

Model	T_s trend (K dec^{-1})	Clear-sky DLRF trend (W m^{-2} dec^{-1})	All-sky DLRF trend (W m^{-2} dec^{-1})	CRE trend (W m^{-2} dec^{-1})
CanESM5	1.25	4.38	3.98	-0.39
CanESM5-CanOE	1.99	6.73	7.16	0.43
CESM2	1.79	5.94	6.31	0.37
CESM2-FV2	2.22	8.41	9.02	0.61
CESM2-WACCM	0.17	1.28	0.42	-0.86
CESM2-WACCM-FV2	0.94	3.59	3.65	0.06
CIESM	0.53	1.98	1.02	-0.96
CMCC-CM2-SR5	1.77	6.52	6.39	-0.13
E3SM-1-1	1.90	7.08	8.18	1.09
FGOALS-f3-L	0.03	1.02	-0.03	-1.05
FGOALS-g3	1.51	4.16	5.56	1.40
GFDL-CM4	1.22	4.35	5.94	1.60
GFDL-ESM4	0.01	0.14	-0.29	-0.43
GISS-E2-1-H	1.01	3.89	2.36	-1.54
MIROC-ES2L	1.85	6.71	7.77	1.06
MIROC6	1.29	3.82	3.59	-0.23
MPI-ESM-1-2-HAM	1.11	3.80	5.84	2.04
MPI-ESM1-2-HR	0.78	2.70	2.22	-0.48
MPI-ESM1-2-LR	1.23	4.61	4.86	0.25

MRI-ESM2-0	1.62	4.16	4.54	0.38
NESM3	1.58	3.87	6.95	3.08
NorCPM1	1.18	4.11	5.98	1.87
SAM0-UNICON	1.07	4.09	4.71	0.62
Ensemble mean (N = 23)	**1.22**	**4.23 ± 0.88**	**4.61 ± 1.15**	**0.38 ± 0.49**
Ensemble median	**1.23**	**4.11**	**4.86**	**0.37**

730 *CRE = all-sky minus clear-sky downwelling longwave flux. Trends are computed from deseasonalized*
731 *monthly-mean anomalies over 1998–2014 by ordinary least squares. T_s is the near-surface (2 m) air*
732 *temperature (tas). Ensemble-mean uncertainties are 95% confidence intervals across the 23 models.*

733